American Mineralogist, Volume 94, pages 1707–1726, 2009

Mechanism of wollastonite carbonation deduced from micro- to nanometer length scale observations

Damien Daval,[1,2,*] Isabelle Martinez,[1] Jean-Michel Guigner,[3] Roland Hellmann,[4] Jérôme Corvisier,[2] Nathaniel Findling,[2] Christian Dominici,[5] Bruno Goffé,[2] and François Guyot[1,3]

[1]Institut de Physique du Globe de Paris, Centre de Recherches sur le Stockage Géologique du CO_2, 4 Place Jussieu, 75005 Paris, France
[2]Laboratoire de Géologie, UMR 8538 du CNRS, École Normale Supérieure, 24 Rue Lhomond, 75005 Paris, France
[3]Institut de Minéralogie et de Physique des Milieux Condensés, CNRS, Université Paris 6 et 7, 140 rue de Lourmel 75252, Paris, France
[4]Géochimie de l'Environnement, Laboratoire de Géophysique Interne et Tectonophysique, CNRS, UMR C5559, OSUG, Université Joseph Fourier, 38041, Grenoble Cedex 9, France
[5]Centre Pluridisciplinaire de Microscopie Electronique et de Microanalyse, Université d'Aix Marseille III, Faculté des sciences de Saint Jérôme, Avenue Normandie Niemen, 13397, Marseille Cedex 20, France

Abstract

The microstructural evolution of $CaSiO_3$ wollastonite subjected to carbonation reactions at T = 90 °C and pCO_2 = 25 MPa was studied at three different starting conditions: (1) pure water; (2) aqueous alkaline solution (0.44 *M* NaOH); and (3) supercritical CO_2. Scanning and transmission electron microscopy on reacted grains prepared in cross-section always revealed unaltered wollastonite cores surrounded by micrometer-thick pseudomorphic silica rims that were amorphous, highly porous, and fractured. The fractures were occasionally filled with nanometer-sized crystals of calcite and Ca-phyllosilicates. Nanoscale chemical profiles measured across the wollastonite-silica interfacial region always revealed sharp, step-like decreases in Ca concentration. Comparison of the Ca profiles with diffusion modeling suggests that the silica rims were not formed by preferential cation leaching (leached layer), but rather by interfacial dissolution-precipitation. Extents of carbonation as a function of time were determined by quantitative Rietveld refinement of X-ray diffractograms performed on the reacted powders. Comparing the measured extents of carbonation in water (condition 1) with kinetic modeling suggests that carbonation was rate-controlled by chemical reactions at the wollastonite interface, and not by transport limitations within the silica layers. However, at conditions 2 and 3, calcite crystals occurred as a uniform surface coating covering the silica layers, and also within pores and cracks, thereby blocking the connectivity of the originally open nanoscale porosity. These crystals ultimately may have been responsible for controlling transport of solutes through the silica layers. Therefore, this study suggests that pure silica layers were intrinsically non-passivating, whereas silica layers became partially passivating due to the presence of calcite crystallites.

Keywords: CO_2 sequestration, wollastonite, carbonation, dissolution-reprecipitation, diffusion modeling, leached layers, FIB-TEM, Rietveld refinement

Introduction

The majority of water-rock interactions in shallow crustal environments occur at non-equilibrium conditions. Mass transfer processes between aqueous fluids and rocks occur in a wide range of geological environments, including surface weathering, the regolith, in streams, waste disposals, aquifers, and even within fractured rocks at depths of several kilometers. Given that water-rock interactions and the re-equilibration of aqueous fluids are never instantaneous, comprehensive efforts have been undertaken over many decades to determine the chemical weathering rates of minerals. The importance of such studies is considerable since chemical weathering processes partly control several geochemical cycles (Lasaga et al. 1994), such as the global C cycle via the CO_2 budget (Berner et al. 1983), and variations in Earth's surface temperature over geological time spans (Walker et al. 1981). Of equal importance, the determination of water-rock interaction rates is necessary for the quantitative modeling of the underground storage and sequestration of anthropogenic gases (see Le Guen et al. 2007 for CO_2), or nuclear radwaste confinement in geological repositories.

To achieve these goals, several complementary approaches have been applied: at a river basin scale, chemical weathering rates have been derived from field measurements based on chemical and isotopic analyses of river waters (Gaillardet et al. 1999 and references therein; Dessert et al. 2003); weathering rates in the field can also be derived from weathering profiles and soil chronosequences (White et al. 2001; Blum and Hellmann, in review); and finally, perhaps the most widely used method is based on the determination of empirical rate laws from laboratory experiments performed on individual minerals (for a review, see chapters 4 to 7 in White and Brantley 1995). Whereas laboratory-based mineral dissolution rate laws are often the ones that are integrated into reactive transport codes for modeling the long-term evolution of mineral assemblages and fluids during

* E-mail: daval@ipgp.jussieu.fr

water-rock interactions (Xu et al. 2004; Knauss et al. 2005), it has been continuously recognized that bridging the gap between laboratory-scale conditions and water-rock interactions in the field is still a challenge. In general, dissolution kinetics measured at far-from-equilibrium conditions in laboratory experiments are much faster than those measured in the field. Discrepancies in dissolution rates of up to four orders of magnitude are evident (Brantley 1992; Swoboda-Colberg and Drever 1993; Drever and Clow 1995; White and Brantley 2003). Thus, the relevance of numerical simulations based on rate laws derived from laboratory experiments can, in many cases, be questioned.

A detailed review of the many possible explanations for such outstanding discrepancies is beyond the scope of this study, and is available in some of the aforementioned papers. Briefly, the main ideas proposed include: (1) Reactions in the field are significantly slower because they often take place at fluid saturation states approaching chemical equilibrium. Furthermore, the effect of fluid saturation (Gibbs free energy of reaction) on the kinetics is perhaps not correctly taken into account by geochemical codes that use rate laws that rely on transition state theory (TST)-based equations (Burch et al. 1993; Lasaga and Lüttge 2001; Hellmann and Tisserand 2006). (2) Solutes that have a strong inhibiting effect (e.g., Al species according to Oelkers et al. 1994) are generally omitted. (3) The effect of "aging" of the mineral surfaces results either from the rapid disappearance of the most reactive high-energy lattice defects or from the passivating ability of protective inorganic secondary phases (Velbel 1993; White and Brantley 2003). With respect to this latter hypothesis, the impact on dissolution rates of secondary phases and/or residual amorphous surface layers produced by incongruent dissolution has been the subject of lively debate for over 50 years. In the early 1970s, the pioneering work of Luce et al. (1972) on the dissolution behavior of Mg-bearing silicates revealed incongruent dissolution, with preferential release of Mg and parabolic kinetics. This was first interpreted and modeled as the consequence of a transport-limited process, where reactants and products diffuse through a leached layer surrounding the dissolving mineral. The problem of linear vs. parabolic kinetics was also extensively debated in that decade by Helgeson (1971, 1972) and Lagache (1976). The experiments of Lagache attributed parabolic kinetics to the degree of solution saturation (i.e., ΔG_r), and not to diffusion-limited transport through surface layers. Moreover, the occurrence of parabolic kinetics observed by Luce et al. (1972) was later attributed to the rapid dissolution of fine surface particles present on the dissolving grains during the first stages of dissolution (Schott et al. 1981). In parallel, the observation that dissolution takes place at selective locations on mineral surfaces, both in laboratory experiments and in the field, led some authors (Berner 1978; Berner et al. 1980; Schott et al. 1981) to suggest that silicate weathering is controlled by surface chemical reactions rather than by diffusion through a leached layer. It is now generally accepted that the dissolution kinetics of silicate minerals is controlled by surface chemical reactions, both in the field and in the laboratory (Kump et al. 2000).

With respect to coatings that are unambiguously identified as secondary precipitates, numerous studies (Nugent et al. 1998; Shih et al. 1999; Cubillas et al. 2005) have reported that their presence may slow down the weathering rate of the underlying phases. Several conceptual models have been proposed to explain how coatings affect dissolution rates. Various parameters were identified as crucial to predict the passivating ability of a given coating, such as (1) the molar volume ratio of product to reactant [i.e., ratio > 1 leading to passivating properties; see Velbel (1993) and Putnis (2002); and original references therein]; (2) the potential crystallographic relationships between coatings and underlying unaltered phases if both reactants and products are crystalline (Cubillas et al. 2005); or (3) if the coating is a silica gel, its potential evolution from a porous structure to a denser and less permeable assemblage due to the progressive condensation of silanol moieties within the silica gel (Casey et al. 1993; Gin et al. 2001; Cailleteau et al. 2008).

The impact of silica coatings on the transport of reaction products to the bulk solution, as well as their mechanism of formation, has been addressed in several recent studies dealing with mineral carbonation reactions (Park et al. 2003, 2004; Giammar et al. 2005; Béarat et al. 2006; Huijgen et al. 2006; Teir et al. 2007; Andréani et al. 2009). Carbonation reactions represent a potentially efficient way of sequestering CO_2 over long time spans because carbon dioxide is then sequestered into a stable solid phase (Oelkers et al. 2008 and references therein). Equation 1 represents a typical carbonation reaction of a M-bearing silicate mineral that dissolves in the presence of CO_2 to yield a M-carbonate and silica (where M is a divalent cation):

$$M_xSi_yO_{x+2y-z}(OH)_{2z} + xCO_2 \rightarrow xMCO_3 + ySiO_2 + zH_2O \quad (1)$$

Although this reaction is often favored thermodynamically, especially in the context of basic and ultrabasic rocks (McGrail et al. 2006), its efficiency may be limited if the reaction is somehow kinetically slowed, which may be the case if the silica coating hinders either the outflux of dissolution products, or the influx of fluid to the reaction front, or both. In most of the aforementioned studies dedicated to mineral carbonation, it was suggested, although neither unambiguously proven nor quantified, that silica gels that form on the reacting grains potentially slow the carbonation process and/or passivate the reaction surface on the primary minerals (Park et al. 2003, 2004; Huijgen et al. 2006; Teir et al. 2007; Andréani et al. 2009). To address this question with respect to Ca-bearing silicates, Daval et al. (2009) compared wollastonite ($CaSiO_3$) carbonation rates measured in batch experiments, with a kinetic model of the process. In aqueous solutions, they showed that the evolution of the measured extents of carbonation as a function of time [$\xi_n(t)$] were close to those predicted using literature-derived wollastonite dissolution rates determined at far-from-equilibrium conditions. Their findings support the idea that the occurrence of thick silica coatings (up to ~100 μm) that formed during carbonation did not prevent the fluid from reaching the pristine wollastonite interface. Their results also suggest that the effect of these coatings on wollastonite dissolution rate was roughly equivalent to that of silica coatings that formed on wollastonite dissolution experiments at far-from-equilibrium conditions in flow-through reactors, although the latter were much thinner (from a few nanometers to hundreds of nanometers) (Xie and Walther 1994; Weissbart and Rimstidt 2000; Golubev et al. 2005; Green and Lüttge 2006; Hellmann 2007). This suggests that wollastonite carbonation is

controlled by surface chemical reactions, rather than by transport limitations within silica layers, either by diffusion in the pore fluid or by volume diffusion in the amorphous solid.

The present study aims to bring new microstructural observations and direct evidence for such assumptions, and to address the effect of secondary phases on carbonation kinetics. Such an approach requires a careful examination of the textural and mineralogical features of carbonation products down to the nanometer scale. In this study, we coupled the focused ion beam (FIB) technique to high-resolution transmission electron microscopy (TEM), a tandem approach which has recently received attention in the Earth science community (Heaney et al. 2001; Benzerara et al. 2005; Wirth 2004, 2009; Lee et al. 2007).

Our investigations are based on direct nanoscale measurements of the chemistry and the structure of altered layers as a function of depth on samples prepared in cross-section. Direct measurement of chemical profiles with nanometer-sized probes avoids artificial broadening of the profiles. Among the first to apply this methodology to study chemical weathering reactions were TEM investigations by Hellmann et al. (2003, 2004).

Materials and experimental methods

Starting materials and experimental setup

A detailed description of the starting materials and the experimental setup can be found in Daval et al. (2009). To summarize, ultrasonically cleaned wollastonite crystals with 125–250 µm grain size and specific surface area of 660 cm^2/g (determined by N_2-BET) were used to perform the carbonation experiments. The investigations were conducted at T = 90 °C and pCO_2 = 25 MPa in small Teflon capsules (volume ~3 mL) capped with porous alumina plugs, and stacked in a Ti-autoclave (18 capsules per run). Although the use of batch reactors for determining accurate rate laws has been extensively criticized (for thorough explanations, see Rimstidt and Dove 1986), arguably they more easily allow the achievement of reaction conditions closer to chemical equilibrium, and are especially useful for examining the coupled effect of silicate weathering and secondary precipitation reactions. Each capsule was filled with a small amount of powder (~300 mg) and either ultrapure deionized water (~0.5 mL), alkaline solution (~0.5 mL, 0.44 *M* NaOH), or no solution. These conditions may be considered as an analog of conditions at the injection well in an aquifer (as reported by Kelemen and Matter 2008; note that alkaline fluids are sometimes encountered in natural environments such as ultramafic rocks), both in aqueous and supercritical CO_2 phases. The entire assembly was then subjected to T = 90 °C and pCO_2 = 25 MPa. At these conditions, CO_2 is supercritical and was free to diffuse across the alumina plugs covering the capsules.

With respect to the samples containing no aqueous solution, the supercritical CO_2 in contact with wollastonite can be considered to be "wet" because it contains a small amount of H_2O that originates from other capsules containing aqueous solutions [see Daval et al. (2009) for details; especially, 7 capsules per run were filled with water only (no wollastonite) to ensure that liquid water was in large excess to saturate the CO_2-rich phase]. More precisely, according to Spycher et al. (2003), at 93 °C and pCO_2 = 202.7 bar (tabulated values of their Appendix A corresponding to the closest to that of the present study), the CO_2 phase contains 14.32‰ of water. Our experimental setup is thus suitable to simulate carbonation reactions that take place in pores of the host rocks that are not saturated with a liquid water phase (Barlet-Gouédard et al. 2007; Rimmelé et al. 2008; Corvisier et al. 2009). As shown in Table 1, carbonation of the wollastonite at T = 90 °C and pCO_2 = 25 MPa led to changes in solution pH; the pH of the pure water decreased and became acidic, whereas the alkaline solution became circum-neutral (nonetheless, we always refer to these as water and alkaline solutions, irrespective of the final pH). Besides, as CO_2 was observed to exsolve very quickly from the liquid phase of the capsules at the end of each run, no attempt was made to determine the in situ pH from measurements of the pH of the corresponding recovered solutions at room conditions. As underlined by Daval et al. (2009), the exsolution of CO_2 is so fast that fluid re-equilibration is always observed, rendering presumably meaningless the final pH measured at ambient conditions.

At last, it was verified that this experimental configuration ensures that the liquid composition of each capsule was not affected by the others [see Daval et al. (2009) for details]. In particular, as Al is a tricky element that may act as an inhibitor of dissolution reactions (Oelkers et al. 1994), it was occasionally verified at the end of experiments that no Al resulting from the potential weathering of the alumina plugs was present in the liquid phases of the capsules. Runs were stopped after different time durations (ranging from 8 h to 11 days) to follow the extent of carbonation as a function of time.

Quantitative determination of extents of carbonation and kinetic modeling

In their previous study, Daval et al. (2009) used two independent techniques to estimate the extents of carbonation as a function of time: solid mass balance and selective acid attack of calcium carbonates followed by the determination of Ca^{2+} released. Despite good agreement between the two techniques, both methods are analytically limited with respect to a detailed characterization of the full range of possible secondary precipitates that can form during carbonation. To improve upon the shortcomings in the previous study by Daval et al. (2009), a Rietveld refinement method was applied in the present study.

Quantification of secondary precipitates by Rietveld refinement of X-ray diffractograms was performed on 15 selected samples used as benchmark materials for which calcium carbonate content was previously determined by mass balance and acid attack. X-ray diffraction (XRD) data were collected with a Rigaku ultraX18HFCE Bragg-Brentano diffractometer equipped with a rotating copper anode (Cu$K\alpha$ radiation). The conditions for generating the X-ray beam were 300 mA and 50 kV. Scans were taken for 2θ ranges from 10 to 70° with 0.01°/s steps, with total accumulation times 100 min. The initial sample preparation procedure followed the methodology given in Raudsepp et al. (1999). Wollastonite powder (200 mg) was ground in absolute ethanol and sieved, retaining the <30 µm size fraction. The powder was then placed in a glass sample holder and pressed against a ground glass slide, and was then serrated with a razor blade in two perpendicular directions to avoid the preferential orientation of grains. This method, however, proved to be inadequate with respect to preventing the preferential orientation of the rod-shaped wollastonite grains. To overcome this problem, instead of using a capillary technique (which can induce significant errors because of sampling bias), a custom-designed apparatus was fabricated, consisting of a PVC plate with 462 mm sized saw-tooth holes (Fig. 1). Wollastonite powder was mounted onto this apparatus, pressed against a ground glass slide, and then reintroduced into the cavity of the initial sample holder in the form of small piles of powder. Although this technique has a drawback in that the Bragg-Brentano conditions are not scrupulously respected (which results in degradation of specimen displacement parameters and broader peaks), overall this technique is superior because the effect of preferred-orientation is avoided, which is the largest source of error.

Rietveld refinement was carried out with the program Fullprof (Rodríguez-Carvajal 2001), following a standard procedure, as can be found in Raudsepp et al. (1999). Peaks were defined as being pseudo-Voigt with a variable percentage of Gaussian-Lorentzian character, and corrected for their asymmetry. The peak full-width at half maximum (FWHM) was varied as a function of the incident angle using a modified version of the empirical expression of Cagliotti et al. (1958); see Rodríguez-Carvajal (2001) for additional details. The profile step-intensity was calculated over an interval of 8 FWHM on either side of each peak centroid. The background consisted of 75 selected points with linear interpolation between them. Starting values for cell parameters, as well as atomic positions and atomic displacement parameters, were taken from previously published crystal structure refinements (compiled in Table 2). Initially, refinements for quantitative phase

Table 1. Chemical characteristics of aqueous solutions used for wollastonite carbonation experiments

	pH (ambient)	pH_i	pH_f	ΔG_r (kJ/mol)
Water	5.83	3.07	4.61	−44
Alkaline solution	12.75	5.62	5.63	−44
Supercritical CO_2	–	nr*	nr*	nr*

Notes: The pH values reported at ambient conditions were measured using a calibrated pH-meter, whereas the values of the starting pH (pH_i) and the final pH (pH_f) at T = 90 °C and pCO_2 = 25 MPa were calculated using the CHESS code and assuming equilibrium between supercritical CO_2 and the aqueous solution (pH_i), as well as equilibrium between supercritical CO_2, the aqueous solution, and secondary calcite (pH_f). The last column indicates the final ΔG_r values of the solutions with respect to wollastonite dissolution after carbonation, calculated with the CHESS code. nr* = not reported (defining pH and ΔG_r for a "wet" supercritical CO_2 fluid is an open question).

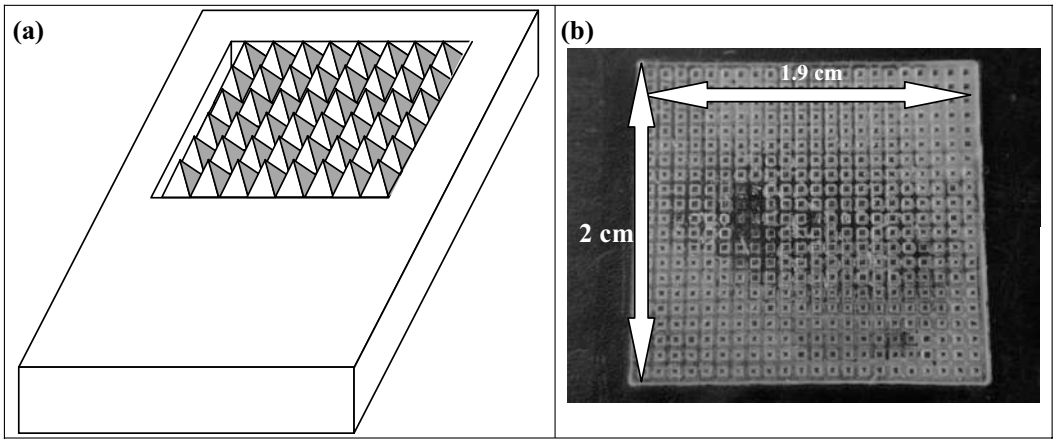

FIGURE 1. (**a**) Schematic representation of the PVC plate designed to randomize the orientations of the wollastonite grains. The powder is subsequently introduced into the cavity of the sample holder by pressing the plate against the sample holder. (**b**) Detailed image of the cavities constituting the PVC plate.

analysis were done using unaltered wollastonite (to estimate the amount of mineral impurities), and using a mixture of unaltered wollastonite and halite (NaCl) as an internal standard. This latter mixture was used to estimate the accuracy of the quantitative-phase analysis and as a reference for the 2θ offset.

A Le Bail refinement with constant scale factor was initially done in the following manner: (1) the surface displacement and the zero delay of the goniometer parameters were refined; followed by (2) the refinement of the unit-cell dimensions of the phases; (3) pseudo-Voigt mixing parameters were refined (η_0 and X), followed by the parameters (U, V, W, and IG) of the modified Cagliotti function; (4) last, the asymmetry parameters of the peaks below $2\theta = 50°$ were refined. This iterative procedure was stopped when the reduced χ^2 reached a minimum or became unstable, with all of the previously cited parameters allowed to vary. All of the parameters were then fixed, subsequently permitting the Rietveld refinement to be performed, leading to refinement of scale factors and atomic positions of the major phases. The quality of the fit between the calculated and observed diffraction-profiles was evaluated using standard indices of agreement, such as the reduced χ^2 index defined by Rodríguez-Carvajal (2001). The quantitative Rietveld refinement of X-ray diffractograms (see Fig. 2 for typical graphical refinements and Table 3) revealed that about 5 wt% of the starting material was composed of quartz. Normalized extents of carbonation (ξ_n) as a function of time were calculated as follows:

$$\xi_n = (x_{Cal}/M_{Cal})/(x_{Wo}/M_{Wo} + x_{Cal}/M_{Cal}) \quad (2)$$

where x_{Cal} and x_{Wo} are the weight percent (dimensionless) of calcite and wollastonite found by Rietveld refinement, and M_{Cal} and M_{Wo} are, respectively, the molecular masses of calcite and wollastonite (g/mol), thus yielding dimensionless ξ_n.

Modeling the extents of reaction was done using the geochemical code CHESS (van der Lee and De Windt 2002), using rate laws taken from the literature for each step of the carbonation process (wollastonite dissolution and calcite precipitation). Major potential discrepancies between experimental data and kinetic modeling, other than those due to intrinsic analytical errors, are attributed to two major sources: (1) transport limitations (CHESS does not incorporate reactive transport) and (2) incorrect mineral dissolution and precipitation rates and/or rate laws; this latter idea was treated in detail in Daval et al. (2009) and will not be discussed further here.

Analysis of the diffraction-line broadening on carbonated powders

To further constrain the mechanisms of carbonate precipitation, the microstructural features of calcite crystals were determined from a detailed analysis of powder XRD patterns. The broadening of Bragg peaks is mainly affected by two contributions: (1) instrumental resolution, and (2) microstructural effects related to the size of the crystallites and to strain. These combined effects can be separated by use of deconvolution methods, such as Le Bail or Rietveld refinements. Powder XRD data were collected under the same experimental conditions as those described previously, but the use of a classical sample holder was preferred to our custom-made design (see Fig. 1), mainly due to the fact that the latter induces artificial peak broadening and degradation of specimen displacement parameters. To mitigate the potential effects of preferred orientation of the grains, only Le Bail refinement (profile matching with constant scale factor) was carried out using the program

TABLE 2. Sources of crystal-structure data used in Rietveld refinements

Mineral	Source
Calcite	Sitepu et al. (2005)
GGG	JCPDS Reference 13-0493 (1963)
Halite	Viswamitra and Jayalakshmi (1972)
Quartz	Hazen et al. (1989)
Wollastonite	Mamedov and Belov (1956)

Fullprof (Rodríguez-Carvajal 2001). The procedure we followed to determine the microstructural features of calcite crystals was similar to a standard method described, for example, in Montes-Hernandez et al. (2008). First, the instrumental resolution function (IRF) of the diffractometer was calculated by performing refinement of an XRD pattern of a strain-free sample [gadolinium gallium garnet (GGG), $Gd_3Ga_5O_{12}$]. The peak shapes were fitted using the pseudo-Voigt profile function of Thompson et al. (1987). The background consisted of selected points with linear interpolation between them. The asymmetry parameters of the Finger correction S/L and S/D (Finger et al. 1994) and the Cagliotti parameters were refined for the standard sample of GGG. All these parameters were then kept fixed during the subsequent refinements of the XRD patterns of the reacted wollastonite powders, such that any further refinement accounted only for microstructural effects (see Martinez-Blanco et al. 2008 for details). With respect to calcite, anisotropic size broadening was modeled in terms of spherical harmonics, allowing the coherent domain average apparent size corresponding to each reciprocal lattice vector to be calculated. The Cagliotti parameter U was refined to account for some isotropic strain in the Gaussian component of the peak profile. Only isotropic coherent domain size and isotropic strain were considered for the two other phases (wollastonite and quartz) because of small amounts of each of these phases in the analysis of the XRD patterns. By performing refinements with different starting values of the previously described parameters, a rough idea of the errors and the stabilities of the results can be estimated. When peak broadening was not limited by instrumental resolution, errors in size were found to be ~30%; errors in strain were less than 10%.

Scanning electron microscopy (SEM)

The powders were studied by SEM (Hitachi S-2500) operating at 15 kV, with a working distance of 25 mm. The samples were either fixed on an adhesive carbon support and gold-coated, or impregnated with epoxy resin, polished, and gold-coated to obtain cross-sections of the grains. Qualitative chemical analyses were acquired by energy dispersive X-ray spectrometry unit of the SEM (EDXS, Thermo Noran Si/Li detector). The acquisition time was generally 90 s, which was the duration necessary to acquire spectra with maximum peaks at ~2000 counts.

Cross-sectioning by the focused ion beam (FIB) technique

Reacted sample grains were initially impregnated in an epoxy resin. Ultrathin electron transparent cross-sections were then cut from three samples, with each one representing one of the three experimental conditions: (1) C3 (t = 2 days, pure water); (2) C6 (t = 2 days, alkaline solution); and (3) E10 (t = 11 days, supercritical CO_2). According to the measurements of Daval et al. (2009), the extents of reaction for all three samples are roughly similar ($\sim 0.5 < \xi_n < \sim 0.8$), due to the much slower kinetics in supercritical CO_2. FIB milling was performed with a FEI Model

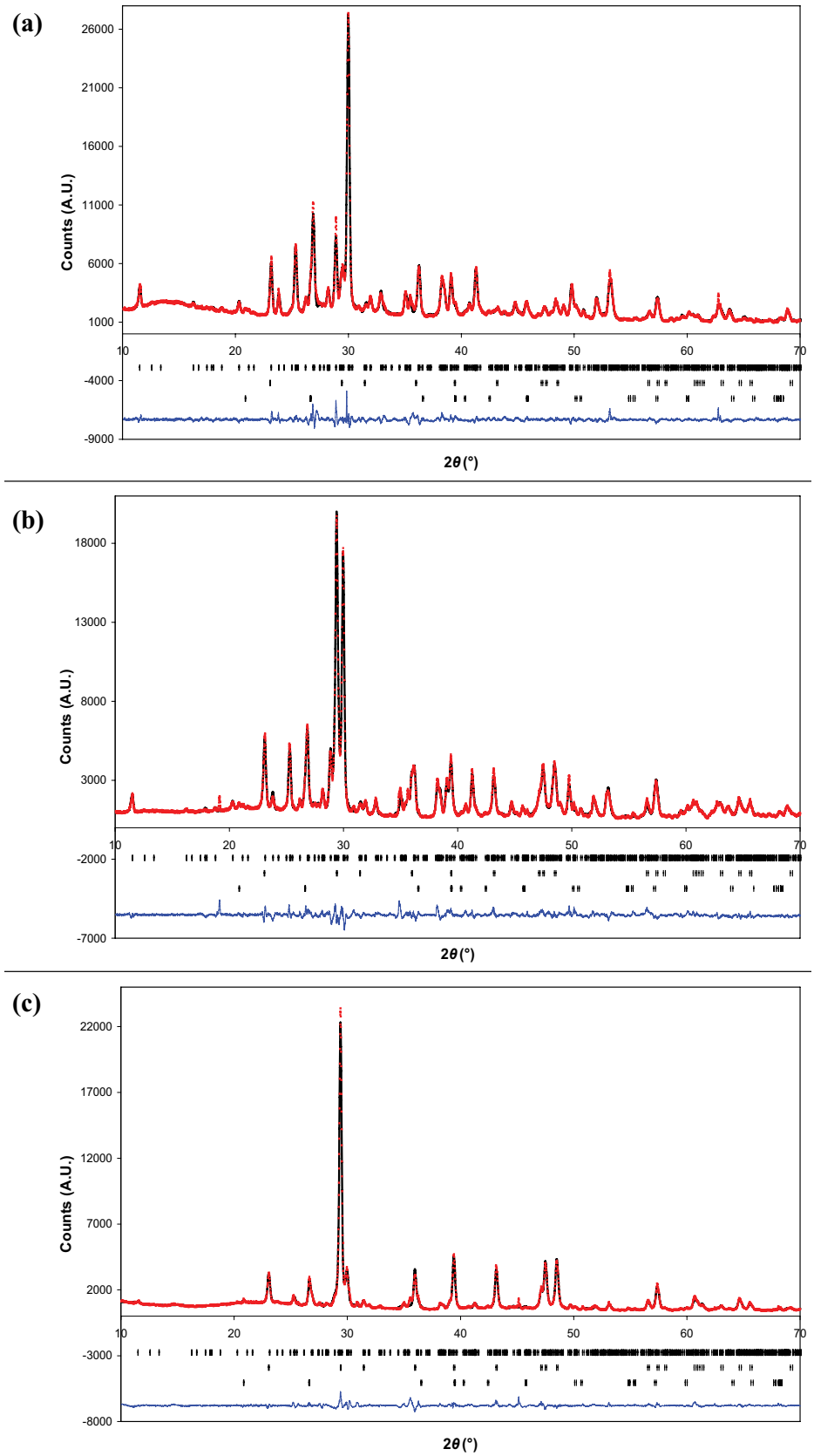

FIGURE 2. Typical graphical results of Rietveld refinements performed on (**a**) sample B9 (wollastonite reacted 1 day in supercritical CO_2, $\xi_n^{RR} = 0.09$), (**b**) sample B4 (wollastonite reacted 1 day in an alkaline solution, $\xi_n^{RR} = 0.50$), and (**c**) sample C3 (wollastonite reacted 2 days in water, $\xi_n^{RR} = 0.83$). The red squares indicate the experimental data points of the diffractogram, the solid black line the modeled diffractogram, the solid blue line the difference between experimental and modeled diffractograms (residue). The vertical black lines indicate the positions of the Bragg reflections. (Color online.)

TABLE 3. Relative abundance of minerals determined by Rietveld refinements for selected powders

Sample	χ^2	Halite	Wollastonite	Calcite	Quartz	ξ_n^{RR}	ξ_n^{AA}	ξ_n^{MB}
Starting materials								
Wo. 1	4.97	–	96.21	0.87	2.92	–	–	–
Wo. 2	4.01	–	95.43	0.44	4.13	–	–	–
90 Wo:10 Hl*	6.62	8.21	87.55	1.24	3.00	–	–	–
50 Wo:50 Hl#	5.87	51.02	45.49	1.18	2.31	–	–	–
10 Wo:90 Hl†	5.94	87.60	11.13	0.26	1.01	–	–	–
Water								
A1	6.67	–	62.78	32.72	4.50	0.38	0.37	0.35
B2	6.10	–	31.57	64.08	4.35	0.70	0.66	0.75
C3	3.23	–	18.95	77.51	3.54	0.83	0.75	0.87
D3	7.08	–	3.59	94.05	2.36	0.97	0.87	0.98
E1	6.55	–	3.31	93.86	2.83	0.97	0.93	0.96
Alkaline solution								
A4	8.55	–	76.01	20.88	3.11	0.24	0.23	0.27
B4	5.33	–	52.81	45.14	2.05	0.50	0.47	0.58
C6	6.75	–	42.42	53.39	4.19	0.59	0.62	0.67
D5	4.91	–	19.15	77.59	3.26	0.82	0.74	0.79
E5	4.02	–	23.30	73.75	2.95	0.79	0.76	0.80
Supercritical CO_2								
A9	6.43	–	89.80	4.98	5.22	0.06	0.06	0.07
B9	3.86	–	88.97	7.26	3.77	0.09	0.12	0.14
C9	5.36	–	76.82	19.14	4.01	0.23	0.23	0.25
D10	7.31	–	39.65	54.67	5.68	0.62	0.60	0.65
E9	10.5	–	57.97	38.12	3.91	0.43	0.51	0.48

Notes: The accuracy of the fit is provided by the χ^2 value reported in the 2nd column. The relative amounts of halite (Hl), wollastonite (Wo), calcite, and quartz are reported in wt%. The reaction time for each sample is labeled by the first letter of the sample's name (experimental durations of 8 h, 1, 2, 5, and 11 days correspond to letters A, B, C, D, and E, respectively). The last three columns report the extents of carbonation calculated using Rietveld refinement (ξ_n^{RR}), acid attack (ξ_n^{AA}), and mass balance (ξ_n^{MB}). Theoretical abundances in prepared mixtures: 90.29 wt% Wo:9.71 wt% Hl*; 50.06 wt% Wo:49.94 wt% Hl#; 10.74 wt% Wo:89.16 wt% Hl†.

200 SEM FIB system. The basic principles of the method are described in Heaney et al. (2001) and in Wirth (2004). The samples were previously carbon-coated to protect the underlying phase during milling. A thin layer of platinum (~1 µm thick) was deposited on the specimen surface before Ga ion milling. A 30 kV Ga^+ beam operating at 20 nA was used to cut the thin section to a depth of ~5 µm. The last step consisted of ion milling at much lower beam currents (~100 pA), to achieve a final thickness of approximately ~80 nm. The ~15 µm × 5 µm × 80 nm thin section was removed from the sample with a micromanipulator and placed onto a carbon-coated copper TEM grid for subsequent TEM analyses.

TEM, EDXS, and electron energy loss spectroscopy (EELS) analyses

High-resolution transmission electron microscopy (HRTEM) and scanning transmission electron microscopy (STEM) observations were carried out on a JEOL 2100F microscope operating at 200 kV, equipped with a field emission gun. STEM observations were performed both in brightfield (BF) and darkfield (DF) modes. EDXS maps were acquired in STEM DF mode, with a focused electron beam (1 nm). EELS spectra were acquired using a dispersion of 0.1 eV/channel to record spectra in the range of 290–392 eV. The dwell time was optimized to acquire sufficient signal intensity and to limit beam damage. Tomography was performed on FIB thin sections using a JEOL 2100 (LaB_6) TEM, operating at 200 kV. Samples were tilted between –40 and +40°, and images were acquired with the DigitalMicrograph software at 1°/step in Saxton-scheme mode. Images were processed using the code TomoJ (Messaoudi et al. 2007). The images were treated with the ImageJ program (Rasband 2002). In addition to investigations on the FIB thin sections, some selected carbonated powders were ground in pure ethanol; drops of the liquid phase containing the smallest particles in suspension were then deposited on a carbon-coated copper grid and observed by TEM.

RESULTS

Quantitative determination of extents of carbonation

Extents of carbonation determined by Rietveld refinement of XRD patterns, listed in Table 3, display similar trends to those reported in Daval et al. (2009). Typical refined XRD patterns are shown in Figure 2. For each starting chemistry (pure water, alkaline solution, supercritical CO_2), ξ_n values level to a plateau after an initial sharp increase during the first days of alteration. The plateaus do not correspond to complete reaction for the experiments in supercritical CO_2 and in alkaline solution, ξ_n being much less than 1 ($\xi_n = 1$ when no wollastonite remains). In general, carbonation is faster in aqueous media than in supercritical CO_2.

To better assess the quality of the intercalibration of the different quantitative techniques, ξ_n values determined by Rietveld refinement (ξ_n^{RR}) are plotted as a function of ξ_n values for the same samples, determined either by mass balance (ξ_n^{MB}) (Fig. 3a) or by selective acid attack of calcite followed by measurement of Ca^{2+} released (ξ_n^{AA}) (Fig. 3b). As illustrated by the correlation coefficient of the linear regression of the corresponding series of data ($R^2 > 0.98$ in both cases), the ξ_n values found using Rietveld refinement are in excellent agreement with the values determined by the two other techniques. These results support the idea that Rietveld refinement is a powerful tool for following the extents of carbonation as a function of time, even when only small amounts of carbonates are present (down to a few weight percent carbonate, i.e., $\xi_n < 0.1$ for wollastonite, see Table 3). Of equal importance, these results also show that the preparation method developed in the present study for avoiding the preferential orientation of the grains can be satisfactorily used to determine mineral abundances in such assemblages. This opens interesting perspectives for the quantification of minerals in complex matrices containing acicular or plate-shaped crystallites, as would be the case, for example, for the carbonation of phyllosilicates such as serpentines.

The slope of the linear regression of ξ_n^{RR} as a function of ξ_n^{MB} is close to 1, but is up to 10% greater than the regressed slope of ξ_n^{RR} as a function of ξ_n^{AA} (as a consequence, the same holds for the regression of ξ_n^{MB} as a function of ξ_n^{AA}; plot not shown). This means that ξ_n values determined by acid attack are systematically smaller than those determined either by Rietveld refinement or by mass balance. Possible explanations are discussed in the next section.

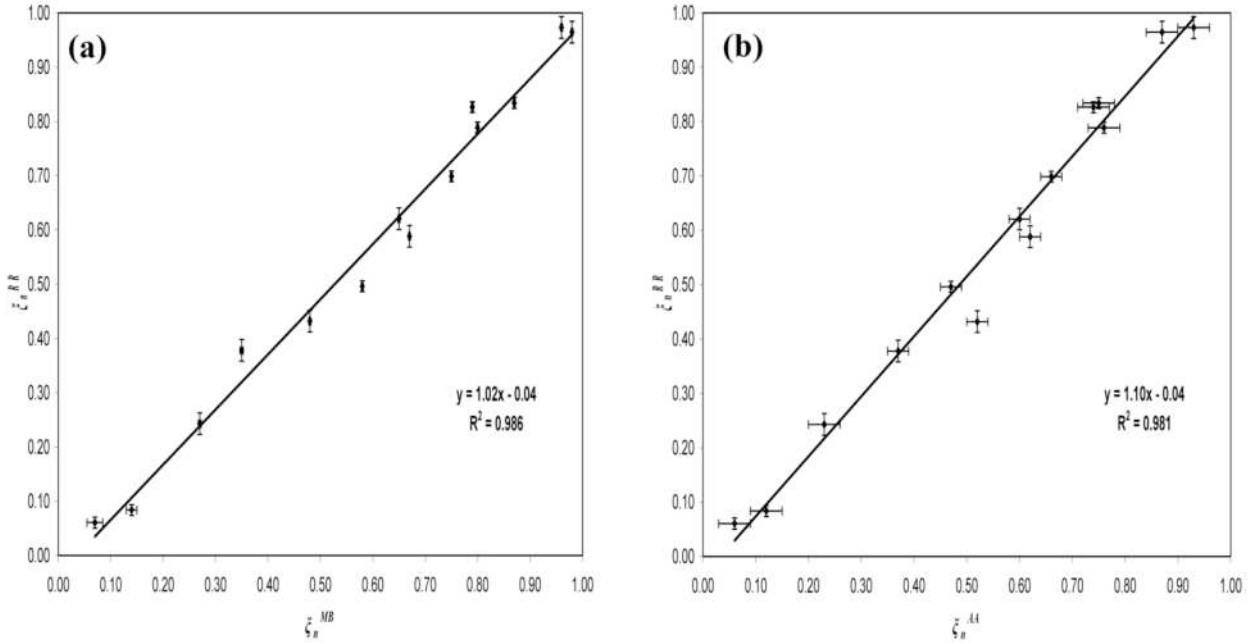

FIGURE 3. Intercalibration plots of the 3 different quantitative methods used to determine extents of carbonation. Extents of carbonation quantified by Rietveld refinement are plotted as a function of (**a**) extents of carbonation quantified by mass balance; (**b**) extents of carbonation quantified by selective acid attack of carbonate minerals.

Textural and chemical characteristics of silica layers, mineralogy, and microstructure of secondary phases

Spatial organization. At the micrometer-scale, wollastonite replacement was observed by SEM to occur pseudomorphically, as the rod-shaped morphology of the reacted wollastonite grains was preserved by the silicon-rich secondary phase for each of the three starting chemistries (Figs. 4a, 5a, and 6a). The secondary silica layers were observed to be systematically spatially adjacent to the unaltered wollastonite cores, regardless of the solution chemistry. At the micrometer-scale, the silica layer is extensive (up to 100 μm thick, Fig. 4a) and mainly (but not completely) free of other phases when the wollastonite was reacted in pure water, whereas it extensively contains (and is covered with) calcite crystals when reacted in alkaline solution and supercritical CO_2 (Figs. 5a and 6a). As illustrated in Figures 4a and 5a, micrometer-sized channels are present within the silica layer; most of these are calcite veins or channels filled with Ca-microcrystallites, which suggests that the bulk solution permeated the silica layer during carbonation. Finally, the exterior regions of the mineralogical assemblages (the free spaces between the grains) are filled with calcite crystals. Whereas large and isolated calcite crystals (up to a few tens of micrometers, Fig. 4a) are associated with the silica layers (surfaces or between individual wollastonite grains) after reaction in water, the two other conditions are characterized by secondary calcite forming compact, continuous coatings on the silica layers (Figs. 5a and 6a). In any case, these calcite crystals shown in SEM images do result from the carbonation reaction, and not from the small amount initially present in the starting materials (~1 wt%, see Table 3). Actually, these impurities were difficult to characterize by SEM in the (pristine) starting powder, and occurred as non-euhedral, micrometer-sized crystals without spatial relation with the wollastonite grains.

Properties of silica layers. Selected area diffraction patterns in TEM showed that the silica layers are amorphous (data not shown; however, this is noticeable in Figs. 4b and 4d). The amorphous silica texture was found to be heterogeneous. A common feature of silica layers formed in each one of the three investigated conditions is their high porosity (Figs. 4b, 5e, and 6d). Elevated porosity values of up to 30% were measured by image analysis in the samples reacted in supercritical CO_2 (Fig. 6d). Since the porosity is heterogeneously distributed in the other investigated samples, an averaged value of porosity is not reported here because this concept is not relevant. This latter idea is illustrated, for example, in Figure 5e where a sharp interface between porous and non-porous amorphous silica is observed. The investigation of the 3 FIB thin sections did not allow us to test whether a spatial correlation exists between high porosity areas and their distance from the interface with the unaltered wollastonite. However, for the samples reacted in the two aqueous solutions, weakly porous zones were often associated with zones with a higher density of cracks with nanometer- to micrometer-lengths and nanometer-diameters (Figs. 5b, 5c, and 5d). Three-dimensional reconstructions based on TEM tomography, such as the one shown in Figure 5d, ensured that pores and veins are present at all depths throughout the FIB thin section, and are clearly distinguishable from superficial damages (left corner of the reconstruction). The cracks were often filled with nanometer-sized calcite minerals (see below), so it is likely that they represent channels that served to transport Ca-rich aqueous fluids between the wollastonite reaction front and the bulk solution. The minor amount of nanometer-sized calcite embedded in the silica matrix may account for the systematic slight difference between ξ_n^{AA} vs. ξ_n^{RR} or ξ_n^{AA} vs. ξ_n^{MB}, since some of these

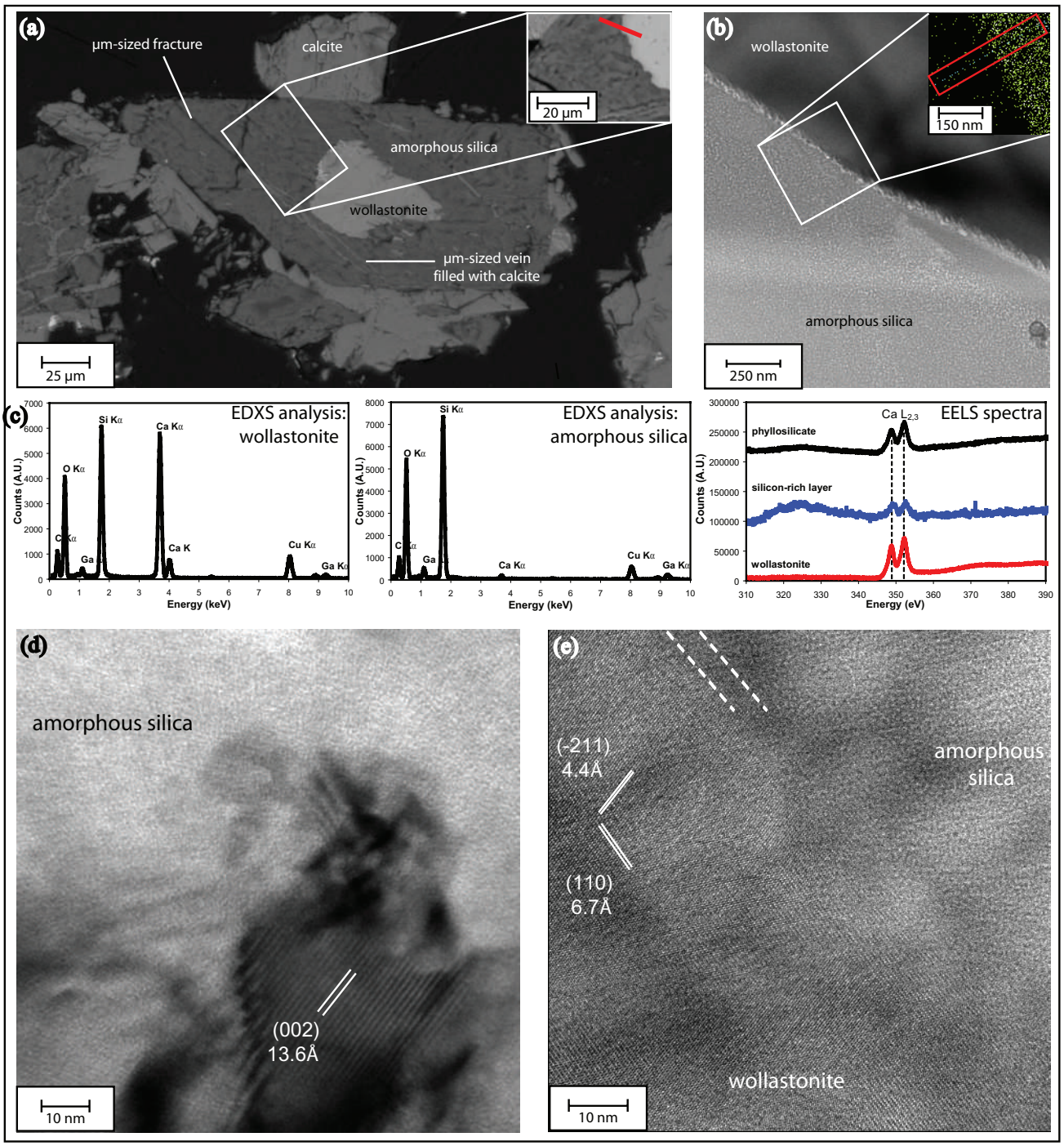

FIGURE 4. SEM and TEM images of wollastonite carbonation in pure water. (**a**) Backscattered electron SEM images of carbonated wollastonite grains in cross-section after 2 days of reaction (sample C3). Wollastonite (white) is surrounded by a fractured, thick silica-rich (dark gray) layer. Exterior calcite crystals (pale gray) are also observed. Inset: Magnification of the location of the FIB thin section extraction (short red line). (**b**) TEM image of the wollastonite- silica interface. Inset: STEM-EDX map of calcium concentration of the corresponding area. Bright area corresponds to higher Ca concentration. Note the sharpness of the interface and the presence of calcium in the silica layer. (**c**) (left) EDXS analysis of wollastonite; (center) EDXS analysis of the silica phase; (right) EELS spectra at the Ca $L_{2,3}$ edge in the Ca-phyllosilicate (black line), in silica layer (blue line), and in wollastonite (red line). (**d**) HRTEM image of Ca-phyllosilicate embedded within silica matrix. The (002) lattice planes were indexed, allowing the space group and cell parameters to be determined (which correspond to plombierite, as determined by Bonaccorsi et al. 2005). (**e**) HRTEM image of the interface that delimits the amorphous altered zone (top right) and crystalline unaltered wollastonite (bottom left). The interface appears to have a slight variable width, up to 5 nm (dotted lines). (Color online.)

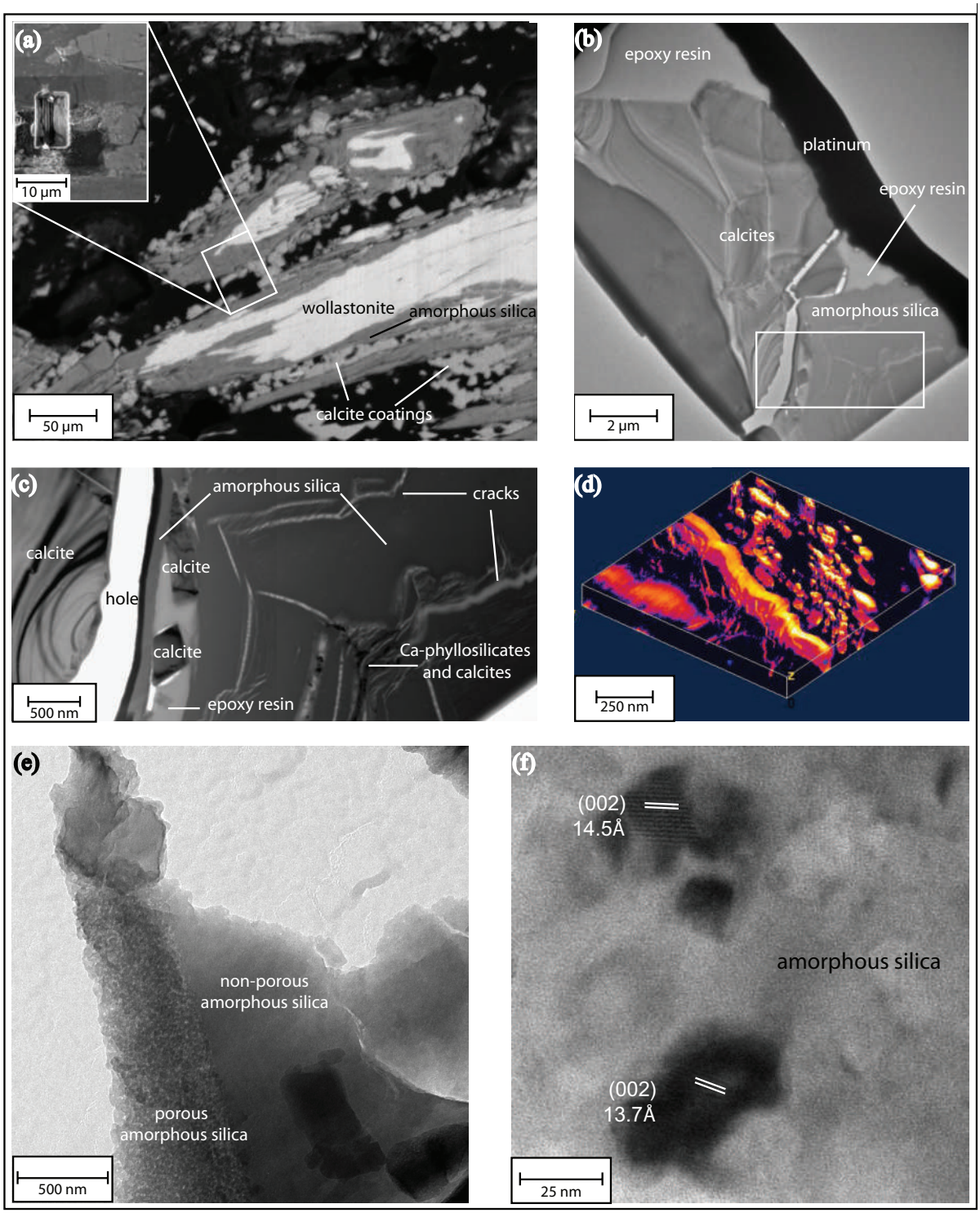

FIGURE 5. Electron microscopy images of carbonated wollastonite grains after reaction in alkaline solution. (**a**) Backscattered electron SEM image of carbonated powders in cross section. Carbonated grain after 2 days of reaction (sample C6). Note the succession of the inner intact cores of unaltered wollastonite surrounded by a fractured layer composed of silica and calcite, and the outer calcite coating. Inset: Magnification of the location of the FIB thin section extraction. (**b**) TEM image of the FIB thin section. Unfortunately, the FIB thin section does not include the wollastonite-silica interface. The white rectangle indicates the area of the fractured layers magnified in **c**. (**c**) TEM image of secondary phases. Note the presence of nanometer-sized cracks, as well as calcite crystals embedded within the silica layer. The tomography was performed on the bottom right corner of this image. (**d**) 3-D reconstruction of the silica layer based on tomography. The fractures and pores are shown in red to yellow colors. Whereas some superficial damage can be evidenced (left corner of the reconstruction), pores and veins are shown to occur at all depths throughout the FIB thin section. (**e**) TEM image showing a sharp interface between porous (left) and non-porous silica (right). (**f**) HRTEM image of Ca-phyllosilicate embedded within the silica matrix. (Color online.)

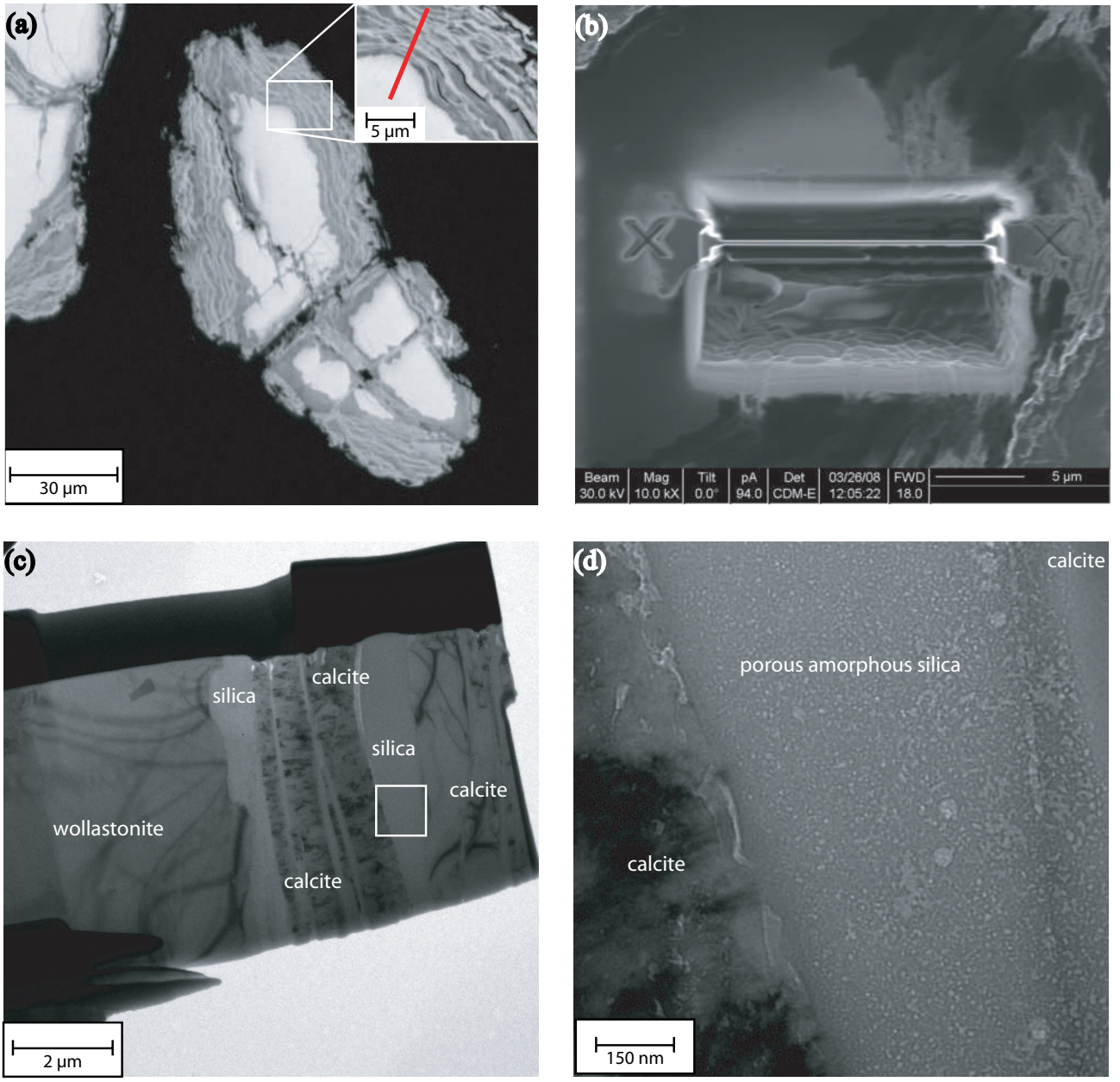

FIGURE 6. General features of wollastonite carbonation in supercritical CO_2. (**a**) Carbonated grain after 11 days of reaction (sample E10). Wollastonite (white) is surrounded by a succession of silica-rich (dark gray) and calcite-rich (pale gray) layers of ~1 µm width. Inset: Magnification of the location of the FIB thin section extraction (short red line). (**b**) Top down view of the FIB thin section before extraction, imaged in FIB apparatus. (**c**) TEM image of the FIB thin section. The white square indicates the location magnified in **d**. (**d**) High-resolution image of the texture of a silica layer between two calcite layers. Despite numerous attempts, it was not possible to identify any Ca-phyllosilicates within that layer of amorphous silica. (Color online.)

crystals may have been less accessible to acid attack compared to the calcite that makes up the precipitated coatings on top of the silica layers. Whether or not these nano- to microcrystallites formed in their entirety during in situ conditions, or were partly formed during the quench phase of the experiments, remains an open question.

The chemical composition of the silica layer was determined at the nanometer-scale by EDXS. A typical EDXS analysis of the silica layer formed during carbonation in aqueous solutions (H_2O, alkaline) is reported in Figure 4c. It reveals that the silica layer is not pure and contains a weak but detectable amount of Ca. This is also the case when the reaction took place in supercritical CO_2. To confirm the calcium signals measured by EDXS, EELS analyses of the silica layer at Ca $L_{2,3}$ edge were acquired, distant from any Ca crystallites present within it. As seen in Figure 4c, the signal unambiguously reveals that the silica layers do contain measurable amounts of calcium. Finally, it was often observed that the TEM beam caused the creation of spherical-like bubbles, which may be due to hydrolysis reactions of free water present in the silica layer (see a similar example in Hellmann 2007).

Evidence for Ca-phyllosilicate formation. A careful investigation of silica layers formed in aqueous solutions revealed that they contain crystals with coherent domain sizes of a few tens of nanometers and inter-reticular distances of ~14 Å. These crystals were either found to be embedded within the amorphous silica matrix (Figs. 4d and 5f) or within cracks that permeated the silica (Fig. 5c). EELS analysis of the crystals shown in Figure 4d at the Ca $L_{2,3}$ edge revealed a significant amount of Ca (Fig. 4c). Taken together, these observations are consistent with the occurrence of plombierite [also named 14 Å-tobermorite, formula: $Ca_5Si_6O_{16}(OH)_2 \cdot 7H_2O$], a calcium silicate hydrate (C-S-H) common in cements and concretes (Maeshima et al. 2003; Bonaccorsi et al. 2005; Richardson 2008). A rough estimate of the relative Ca-phyllosilicate abundance within the silica layer formed during carbonation in aqueous solution was determined using TEM tomography and yielded values of 0.5 ± 0.3 vol%. Ca-phyllosilicates were not observed in the samples reacted in supercritical CO_2.

Microstructure of calcite crystals. The average coherent domain size and the maximum strain along each reciprocal lattice vector of calcite crystallites from carbonated powders after 11 days of reaction were determined and are reported in Table 4. On the whole, the maximum strain was found to be weak to non-existent for samples reacted under all three conditions. As a consequence, broadening of peaks, if present, is mainly due to the limited coherent domain size of the crystallites. Whereas the calcite crystallites formed during the course of experiments in water have such large coherent domain sizes that the broadening of the reflections is indeed limited by instrumental resolution, the calcite crystallites are significantly smaller when formed in alkaline solution and in supercritical CO_2. For the latter case, the average apparent size was ~150 nm, with an average anisotropy of ±96 nm, which is in reasonable agreement with TEM observations that showed calcite crystals with dimensions of a few hundreds of nanometers. These results suggest that for equivalent extents of reaction, calcite formation is mainly driven by the growth of relatively few calcite nuclei when the reaction is initiated in water, whereas the density of nuclei is much more important for the two other conditions. In general, these results are in agreement with the qualitative SEM observations that showed that the largest euhedral calcite crystals grew during carbonation in water.

Wollastonite/silica interface. Consistent with previous studies on silicate mineral weathering at acidic pH (Hellmann et al. 2003, 2004; and references therein; Hellmann 2007), HRTEM revealed that the structural interface between the amorphous altered zone and crystalline wollastonite is abrupt and sharp, varying from 1.5 to 5 nm in width (Fig. 4e). This variation may be due to variable degrees of sub-parallel orientation of the interfacial boundary with respect to the electron beam. The chemistry of the interfacial region was examined by STEM-EDXS, which provided a 2-D spatial distribution of Ca (inset in Fig. 4b). For the samples reacted in the aqueous solutions and in supercritical CO_2 (map not shown), sharp, step-like changes in the concentration of Ca were evidenced. In each case, the interface between the unaltered wollastonite and the silica was characterized by a sharp chemical boundary that was spatially commensurate with the abrupt crystalline-amorphous structural transition. Chemical profiles across and perpendicular to the interfacial regions (dark line in Fig. 7 for reaction in water, dark line in Fig. 8 for reaction in supercritical CO_2; the other curves correspond to diffusion modeling results, discussed below) show that the Ca concentration jumps have a negligible thickness (<25 nm) compared to the total thickness of the amorphous phase (>20 μm for silica formed in water, ~1 μm for silica formed in supercritical CO_2). Similar results were recently reported for acid-pH altered plagioclase feldspar, with Ca, Al, Si, and O gradients even sharper (<10 nm) by Hellmann et al. (2003, 2004). Possible explanations for such minor differences could be that Hellmann et al. (2003) used energy-filtered transmission electron microscopy (EFTEM) to determine concentration profiles across the interfacial boundary; this technique has a better spatial resolution than

TABLE 4. Results of diffraction-line broadening on carbonated powders

	E1		E5		E9	
hkl	Coherent domain size (nm)	Maximum strain (%%)	Coherent domain size (nm)	Maximum strain (%%)	Coherent domain size (nm)	Maximum strain (%%)
012	r.l.	r.l.	r.l.	r.l.	214	4.67
104	r.l.	r.l.	1231	0.34	132	4.67
006	r.l.	r.l.	60	0.34	r.l.	r.l.
110	r.l.	r.l.	130	0.34	64	4.67
113	r.l.	r.l.	445	0.34	133	4.67
202	r.l.	r.l.	113	0.34	76	4.67
024	r.l.	r.l.	r.l.	r.l.	214	4.67
018	r.l.	r.l.	333	0.34	155	4.67
116	r.l.	r.l.	r.l.	r.l.	179	4.67
211	r.l.	r.l.	123	0.34	66	4.67
122	r.l.	r.l.	201	0.34	80	4.67
10 10	r.l.	r.l.	125	0.34	161	4.67
214	r.l.	r.l.	179	0.34	105	4.67
208	r.l.	r.l.	1231	0.34	132	4.67
119	r.l.	r.l.	r.l.	r.l.	139	4.67
125	r.l.	r.l.	r.l.	r.l.	170	4.67
300	r.l.	r.l.	130	0.34	64	4.67
00 12	r.l.	r.l.	60	0.34	500	4.67
217	r.l.	r.l.	792	0.34	158	4.67

Notes: The table shows the average coherent domain size and the maximum strain along each reciprocal lattice vector of calcite crystallites from carbonated powders after 11 days of reaction. The strain is given in %%: a strain of x%% denotes a strain ratio of $\varepsilon = (d_i - d_f)/d_i \times 10\,000$; d_i and d_f being the strain-free crystallite size and the strained crystallite size, respectively. r.l. is reported in the table when the broadening of the reflections is resolution limited. The χ^2 values for the refinement of the diffractograms of E1, E5, and E9 powders are 8.54, 2.21, and 3.37, respectively.

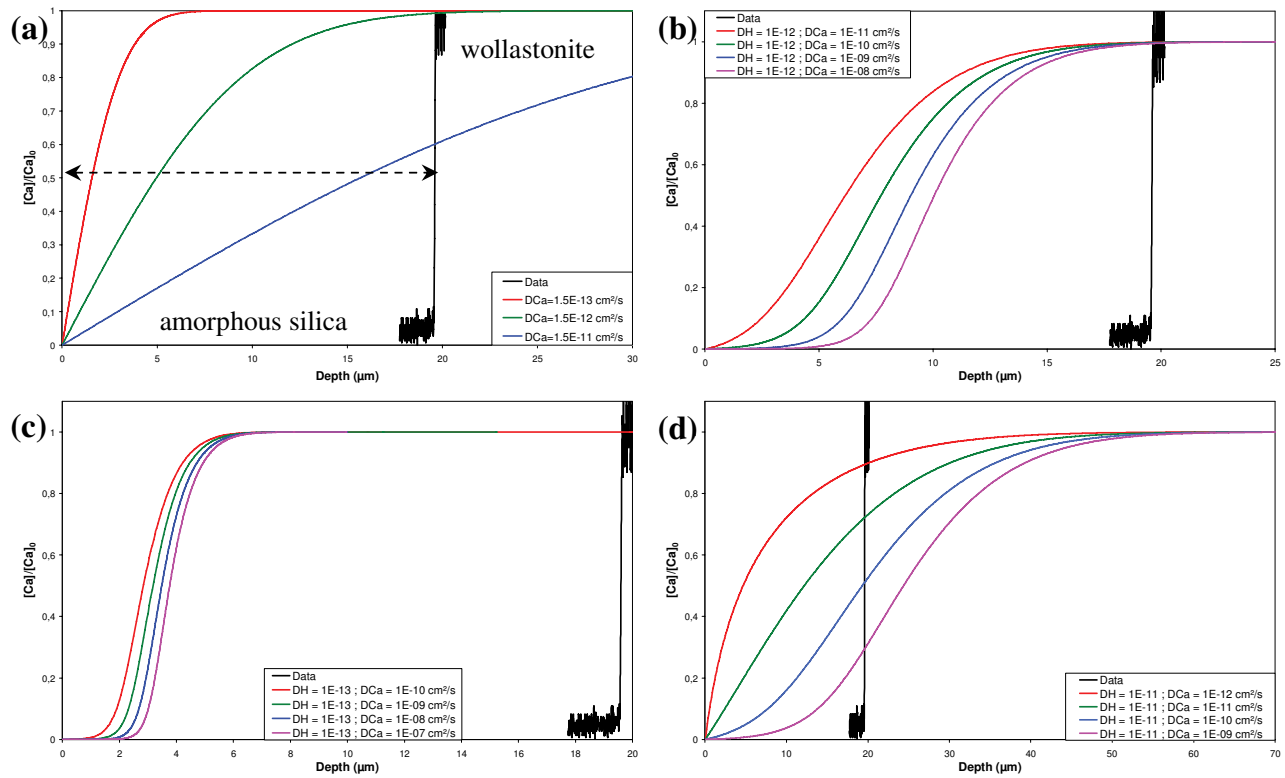

FIGURE 7. Comparison of measured Ca concentration profiles across the silica layer of the sample reacted in pure water (black line) with modeled diffusion curves (colored lines). The Ca concentration is normalized to 1 in wollastonite. The dotted arrow in **a** represents the actual depth of the silica layer. Whereas the simulated curves in **a** were generated using a constant Ca diffusion coefficient, the curves in **b**–**d** were obtained using a Ca^{2+}-H^{+} interdiffusion coefficient, $\widetilde{D}$—see text for details. (Color online.)

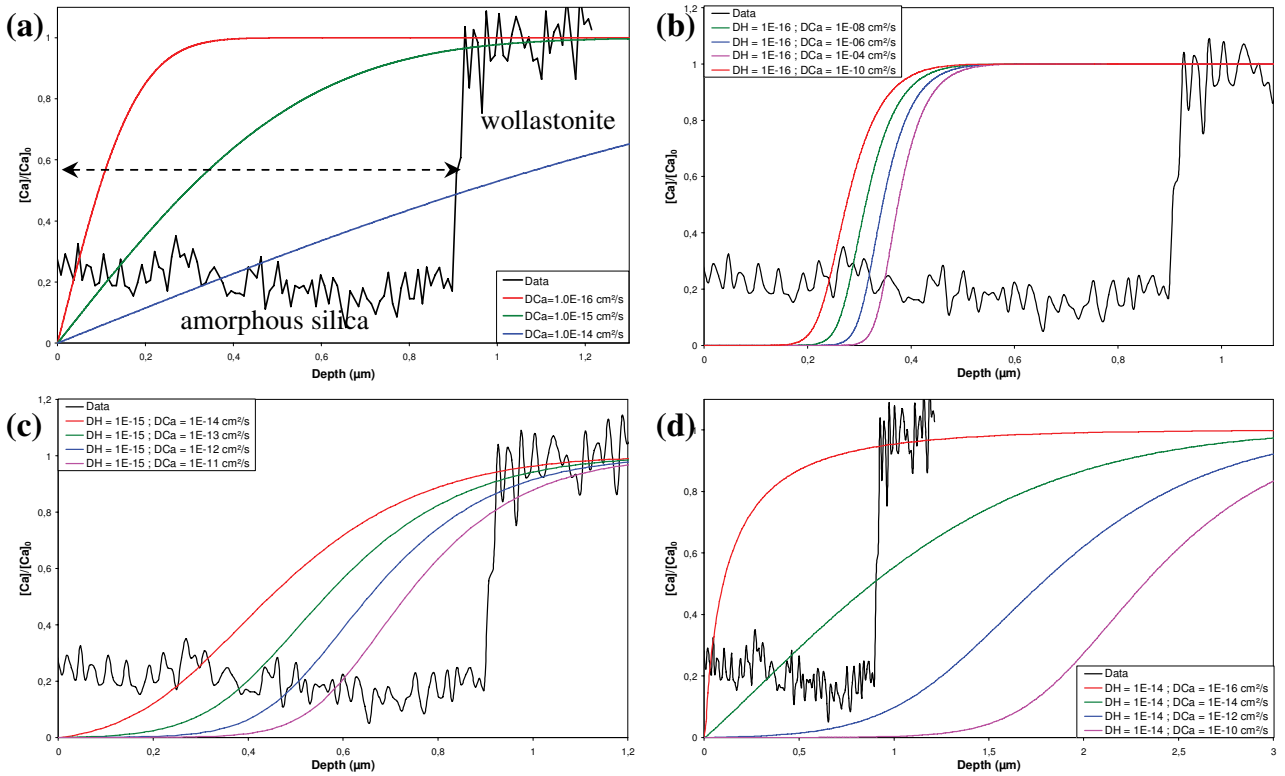

FIGURE 8. Comparison of measured Ca concentration profiles across the silica layer after reaction in supercritical CO_2 (black line) with modeled diffusion curves (colored lines). The concentration is normalized to 1 in wollastonite. The dotted arrow in **a** represents the actual depth of the silica layer. Whereas the simulated curves in **a** were generated using a constant Ca diffusion coefficient, the curves in **b**–**d** were obtained using an interdiffusion coefficient, $\widetilde{D}$. (Color online.)

STEM-EDXS. This implies that the Ca gradient is possibly even sharper than measured. Nonetheless, these small differences in chemical gradients have no effect on the interpretation of the reaction mechanisms, discussed below.

DISCUSSION

Kinetic modeling of wollastonite carbonation and transport properties of silica layers

Carbonation in water. To determine whether or not secondary phases affected carbonation rates in water, measured extents of carbonation were compared with kinetic modeling of the process. The major rate-controlling steps for carbonation were based on data taken from previously published studies on the dissolution and precipitation kinetics of wollastonite (Weissbart and Rimstidt 2000) and calcite (Shiraki and Brantley 1995), respectively. The rate constant (k_{25}) and pH-dependence (n) of wollastonite dissolution at 25 °C were taken from the study by Weissbart and Rimstidt (2000), which contains, as far as we know, the most complete data set published on wollastonite dissolution at acidic pH conditions. For a thorough discussion of the rate laws available in the literature, as well the rate laws and data used here, see Daval et al. (2009). The rate constant at 90 °C (k_{90}), which to date has not yet been determined, was extrapolated from the average of the activation energies from two other wollastonite dissolution studies: Murphy and Helgeson (1989) and Rimstidt and Dove (1986). With respect to modeling the precipitation rate of calcite, we referred to the study of Shiraki and Brantley (1995), and specifically, we used their second rate law, which is based on a surface adsorption mechanism (justification discussed in Daval et al. 2009). The precipitation of amorphous silica was assumed to occur much faster than either of the two other reactions, and therefore its formation can be considered to be instantaneous as soon as the fluid becomes saturated with respect to this phase (see discussion below).

The reactive surface area of wollastonite was assumed to follow a shrinking core model (see van der Lee and De Windt 2002 and Daval et al. 2009 for details). This assumption is in reasonable agreement with SEM observations: as evidenced in Figures 4a, 5a, and 6a, at a micrometer-scale, wollastonite was roughly homogeneously weathered, rather than selectively etched. The initial surface area was based on N_2-BET measurements of the unaltered wollastonite grains (see methods). The evolution of reactive surface area *was not* used as a fitting parameter (as is often the case in the literature), such that the model is independent from the experimentally measured extents of carbonation. We can consider that the time needed for carbonation to be achieved (t_c) is the sum of the three following contributions: (1) time required for complete wollastonite dissolution (t_d); (2) transport of the aqueous products (t_t); and (3) calcite precipitation (t_p),

$$t_c = t_d + t_t + t_p. \quad (3)$$

However, since the kinetic modeling does not include transport terms, this implies that $t_t = 0$ during the course of the simulation. The degree to which this assumption is reasonable can be determined by comparing the experimentally measured extents of carbonation to the modeled curve (Fig. 9). If the experimental data overlap the modeled curve, this can be used

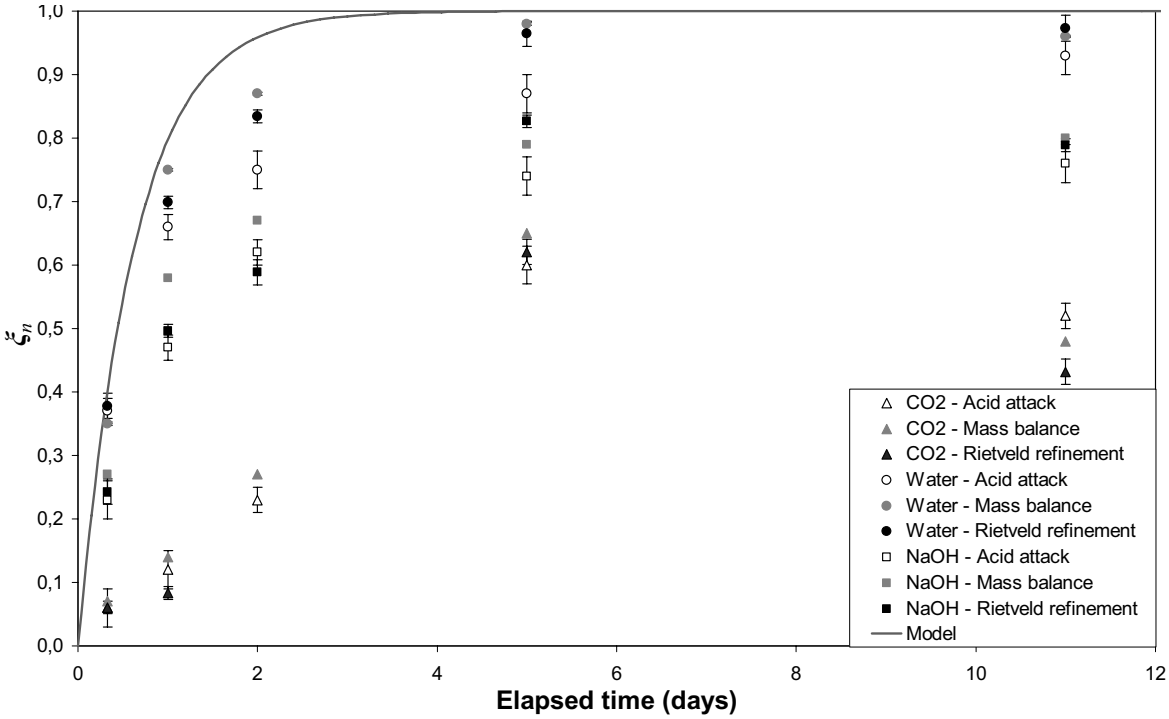

FIGURE 9. Extents of carbonation determined as a function of elapsed time for each of the 3 investigated conditions. The measured extents of carbonation are represented by symbols (see legend for details). The solid gray line represents the kinetic modeling of aqueous (water, alkaline solution) wollastonite carbonation. The divergence of the data from the modeled curve could indicate that the passivating ability of the calcite coatings is more important in supercritical CO_2 than in alkaline solution.

as evidence that transport of reactants and products to/from the reactive interface is not rate-limiting.

Figure 9 illustrates that the measured extents of carbonation in water, based either on mass balance or on quantitative Rietveld refinements of XRD, are close to the modeled curve. This can be considered as a good argument in favor of only a minor effect of the secondary phases on the transport of reactants. Therefore, the effect of the formation of thick silica coatings (up to a few tens of micrometers) surrounding the unaltered wollastonite cores is roughly indistinguishable from that of thin silica coatings which are formed on wollastonite dissolved in mixed-flow reactors at far-from equilibrium conditions. Evidence in the present study, based on the observed microstructure of the silica layer, is consistent with this. The presence of micrometer-sized channels, sometimes filled with carbonates (Fig. 4a), as well as the nano-porous structure of the silica gel (Fig. 4b), suggest that these thick silica coatings do not passivate the wollastonite surface, such that there is no kinetic inhibition of reactant and product fluxes between the reaction front and the bulk solution. Moreover, we cannot discount dehydration effects (and subsequent partial pore closure, see Cailleteau et al. 2008) that may have occurred during quenching (termination of experiment), and thus, the true in situ porosities may even have been greater than those observed by TEM.

Pseudomorphic replacement of wollastonite by porous silica can be explained within the framework of the model discussed by Putnis and Putnis (Putnis et al. 2005; Putnis and Putnis 2007; Kasioptas et al. 2008, see also review in Putnis 2002), whereby the silica is formed by coupled dissolution-precipitation (arguments in favor of such a mechanism are developed in the section "mechanism of silica layer formation"). According to these authors, if the reaction of solid phase $A \rightarrow$ solid phase B occurs, and if: (1) there is a "molar deficit" (more moles of A are dissolved than B precipitated) and (2) $V_B/V_A < 1$ (where V_B and V_A represent the molar volumes of phases B and A, respectively), then the secondary phase B is predicted to be more porous than phase A. These two conditions were satisfied for the case of wollastonite replacement by amorphous silica. Moreover, the porous microstructure of the silica layer, as observed by electron microscopy, is consistent with permanent contact of bulk fluid with the reactive surface of wollastonite, thus showing that the silica layer did not have a significant passivation effect. A similar example, based on the hydrothermal dissolution of albite at acid pH, shows the formation of a porous, 0.5 mm thick rind of boehmite crystals that had no effect on the release rate of silicon from the parent mineral (Hellmann et al. 1989).

The results of the present study are consistent with the idea that wollastonite carbonation in water is not dramatically slowed by the formation of thick silica layers. As a consequence, the major impact of rapid precipitation of silica on the extent of carbonation is that it maintains the dissolution reaction away from equilibrium at a constant, negative ΔG_r (see values in Table 1), thus promoting the dissolution process. As noticed in previous studies (Putnis 2002), this means that there is a "cooperative" autocatalysis effect.

Carbonation in alkaline solution. Even though the carbonation reaction in the alkaline solution occurred at a higher pH range compared to carbonation in pure water (see Table 1), the extents of carbonation determined for these conditions can be directly compared with the same modeled curve in Figure 9 because the rate law determined in Weissbart and Rimstidt (2000) is pH independent over the range of 2–6 ($n = 0$). As pointed out in Daval et al. (2009), other values of n are available in the literature (Golubev et al. 2005), but are small in any case ($n \leq 0.28$). However, unlike carbonation in water, there is a lack of agreement between the modeled curve and the data. As the extent of carbonation attained a plateau value less than unity (~0.8), a possible explanation is that at these conditions the silica coating acted as a partially passivating layer. Surprisingly, however, the chemical, structural and textural properties of silica layers formed under these conditions were the same as those evidenced previously, namely micrometer- to nanometer-sized cracks (Figs. 5a, 5b, 5c, and 5d) and a nano-porous silica layer (Fig. 5e). The lower degree of reaction progress attained in alkaline solution may be due to two non-exclusive reasons: the dense, continuous coating of small calcite crystals (see XRD results and SEM images) that formed on top of the silica layer or, alternatively, the presence of calcite crystals that formed in the nanometer- and micrometer-sized cracks and pores of the silica rind. This suggests that pure silica layers do not passivate (carbonation in water), but the presence of precipitated crystallites may progressively change the transport properties of the layers, rendering them at least partially passivating. The analysis of the diffraction-line broadening of the carbonated powders (Table 4) supports both of the two proposed explanations. Specifically, the diffraction-line broadening revealed that the calcite crystallites are smaller when formed during carbonation in alkaline solution. Thus, for an equivalent extent of carbonation, crystallites are more numerous than in samples reacted in water. Supporting this, TEM observations revealed that the presence of nano-calcite crystallites within the silica layer were more prevalent compared to when carbonation occurred in pure water. Thus, the overall effect of the calcite crystallites may be due both to their presence as a separate coating, as well as a filling material in the cracks and in the nano-porosity of the silica layer.

If the size of the calcite crystals is a key factor in predicting their ability to affect the transport of reactants and products to/from the reactive wollastonite surface, it is important to understand the origin of such differences. One possible explanation is based on the idea that the size of the calcite crystals is controlled by the size of the critical nuclei, which is a function of pH. We hypothesize that in the alkaline solution (higher pH), smaller crystal sizes are favored, thereby facilitating their nucleation and the subsequent filling in of the silica pores by the calcite crystallites (see derivation in Appendix A[1]).

Carbonation in supercritical CO_2. The temporal evolution of the extents of carbonation in supercritical CO_2 display features similar to that described in section above. However, as shown in

[1] Deposit item AM-09-053, Appendices A and B. Deposit items are available two ways: For a paper copy contact the Business Office of the Mineralogical Society of America (see inside front cover of recent issue) for price information. For an electronic copy visit the MSA web site at http://www.minsocam.org, go to the American Mineralogist Contents, find the table of contents for the specific volume/issue wanted, and then click on the deposit link there.

Figure 9, the extent of carbonation in the supercritical CO_2 fluid was much less than in the alkaline solution ($\xi_n \sim 0.5$), as well as in water. If passivation seems to be a likely explanation for the observed trends of the extents of reaction (the calcite coatings being even more compact and continuous than in alkaline solutions), it is difficult to address this with the same arguments as already presented, due to the particularity of carbonation in the assumed absence of an aqueous solvent. It is possible that interaction with a "wet" supercritical CO_2 fluid occurs via a thin H_2O film that interacts with the wollastonite. On one hand, our experimental setup ensures that water is not the limiting reactant, as the amount of dissolved water in the CO_2-rich phase is buffered by the liquid water present in the autoclave. On the other hand, its supply to the pristine interface could be limited as well as that of CO_2 by the presence of passivating calcite coatings. However, because substantiating this idea is beyond the scope of this study, we prefer not to directly compare the experimental extent of reaction data with kinetic modeling (using reaction rates in aqueous solvents from the literature). In addition, the extents of carbonation were not as reproducible as were the carbonation reactions in water and alkaline solution (see details in Daval et al. 2009), perhaps being due to localized grain surface heterogeneities (hydration state of grain boundaries).

If one supposes that, similarly to alkaline conditions, carbonation of wollastonite in "wet" supercritical CO_2 is limited by the access of reactants (CO_2, H_2O) to the pristine wollastonite surface, then the occurrence of a succession of several layers could seem surprising. This would mean that a single layer is not passivating enough to stop the reaction progress. Indeed, it is likely that the diffusivity in a supercritical phase is larger than that in a liquid phase, because of the difference between fluid viscosities (see similar features and explanations for carbonation of serpentine samples in Dufaud 2006). Several layers would thus be required before preventing the reactants to reach the silica/wollastonite interface.

In any case, the mechanism of carbonation of supercritical CO_2 fluids warrants further study. Results from Montes-Hernandez (2009) reveal that "dry" supercritical CO_2 fluids do not react with silicate minerals. Small amounts of water present in supercritical CO_2 fluids (as in this study) are needed to hydrolyze the bonds of minerals, perhaps via a thin water film. Possibly, the carbonation reaction in supercritical CO_2 was ultimately limited by the availability of water at the wollastonite interface in the present study. For this reason, we suggest that detailed experiments of wollastonite weathering and/or carbonation in CO_2 fluids with controlled water fugacities would be a fruitful area of research, and could provide information on the dependence of reaction rates on water fugacity in supercritical CO_2 fluids.

Mechanism of silica layer formation

The thick, continuous, and pervasive silica coatings that surround unaltered wollastonite grains display pseudomorphic features typically associated with residual surface layers resulting from the incongruent dissolution of silicates (Huijgen et al. 2006). Incongruent dissolution, due to the preferential release of certain cations from the parent mineral, leads to the formation of so-called "leached layers." Their formation is thought to be a consequence of the facile exchange of interstitial cations with protons from the bulk solution, and of the fact that M-O-Si bonds are more easily hydrolyzable than Si-O-Si bonds (specifically at acid pH). According to this conceptual model, silicate weathering is a function of two distinct, parallel processes: solid-state volume interdiffusion within the leached layer of preferentially released cations and protons from the bulk solution, and hydrolysis reactions that release Si and O from the fluid/leached layer interface. The leached layer mechanism has been the accepted theory for multi-cation mineral dissolution for over 40 years (Helgeson 1971; Berner and Holdren 1979; Chou and Wollast 1984; Casey et al. 1988; Petit et al. 1990; Hellmann et al. 1997), and it continues to hold sway in the mineral dissolution literature (Chaïrat et al. 2007). Cation and hydrogen depth profiles of altered layers that are sigmoidal and anticorrelated, obtained by surface ion and electron beam techniques, have been the principal argument used to support the idea of solid-state interdiffusion and leached layer formation (Casey et al. 1988; Petit et al. 1990; Hellmann et al. 1997; Schweda et al. 1997; see also diffusion modeling in Hellmann 1997). However, a few recent studies have used a different analytical approach to investigate altered surface layers, based on direct nanoscale structural and chemical measurements of altered zones prepared in cross-section, either by ultramicrotomy or by FIB. This avoids potential artifacts associated with chemical depth profiles obtained indirectly by surface ion and electron beam methods characterized by low lateral spatial-resolution (Hellmann et al. 2003, 2004).

In the present study, we obtained novel nano-scale measurements that are characterized by spatially coincident and sharp, step function-like changes in the structure and chemistry of interfacial regions separating the amorphous altered layer from the unaltered wollastonite parent. To test whether these sharp interfacial chemical gradients, measured by STEM-EDXS analyses (dark lines in Figs. 7 and 8), were compatible or not with the leached layer mechanism, diffusion modeling was carried out. The general diffusion Equation 4 below accounts for the outward diffusion of species within the silica layer (extending from the wollastonite reaction front to the exterior boundary of the silica layer) (Doremus 1975):

$$\frac{\partial C}{\partial t} = \frac{\partial}{\partial x}\left(D\frac{\partial C}{\partial x}\right) + a\left(\frac{\partial C}{\partial x}\right) \quad (4)$$

In the above equation, t is time, C is the normalized concentration of the element chosen ([Ca]), x is the depletion depth (measured from the fluid–solid interface), D the diffusion coefficient of the chosen species (D_{Ca}), and a is the rate of retreat of the fluid–solid interface. As revealed by SEM, the silica coatings preserve the initial rod-shape morphology of the wollastonite grains. It is therefore highly likely that, as soon as the fluid becomes saturated with respect to amorphous silica [note that the fluid analyses performed by Daval et al. (2009) at the end of each experimental run are consistent with this statement], the outer interface of the assemblage (the fluid/silica interface) does not dissolve anymore. As a consequence, it is reasonable to set a to 0. In addition, the diffusion equation is assumed to satisfy the following boundary conditions (note that concentrations are normalized to the bulk concentration): at $x = 0$, $C = 0$, and at $x = \infty$ (the leached layer/bulk interface), $C = 1$, and $\partial C/\partial x = 0$. These

boundary conditions are in good agreement with the measured chemical profiles of Ca; see also additional details in Hellmann (1997). With these boundary conditions, the solution to the above expression using a Laplace transform method (Crank 1990) is:

$$C = 1 - erfc(x / \sqrt{D_{Ca} \cdot t}) . \quad (5)$$

Figures 7a and 8a show the calculated profiles for Ca concentration as a function of depth, based on the above equation. Each figure shows several diffusion profiles, corresponding to a constant diffusion coefficient, D_{Ca}, which ranges from 1.5×10^{-13} to 1.5×10^{-11} cm²/s for carbonation in an aqueous phase, and from 10^{-16} to 10^{-14} cm/s for carbonation in supercritical CO_2. Strikingly, the form of the calculated curves (monotonic increase of Ca from the leached layer/fluid interface to the leached layer/bulk interface) does not resemble the change in the concentration of Ca measured experimentally. This mismatch has been observed in previous studies (see Hellmann 1997, and references therein) and was attributed to modeling the diffusion process with a constant diffusion coefficient, as in Equation 4. Alternatively, the use of a non-constant diffusion coefficient, which varies as function of the concentration (and thus, of depth), could better reproduce profiles with more complex shapes (more or less sigmoidal, with variable sharpness of the concentration gradient). Assuming that the outward diffusion of cations M^{n+} from the bulk mineral and the inward diffusion of H^+ are not independent, but rather are coupled by an ion exchange reaction between H^+ and M^{n+} species, has led some authors to take into account this interdependency by the use of a non-constant, single interdiffusion coefficient, $\widetilde{D}$ (Baucke 1974; Doremus 1975; Hellmann 1997). This interdiffusion coefficient depends on the diffusion coefficients of H^+ (D_H) and M^{n+} (for wollastonite, D_{Ca}) species. The details of the numerical resolution of such a problem can be found in Appendix B[1].

Considering the wollastonite sample reacted in pure water, the results of the simulations using this model are represented in Figures 7b, 7c, and 7d. Each figure shows several diffusion profiles, each one with a constant value of D_H (ranging from 10^{-13} to 10^{-11} cm²/s), and different values of D_{Ca}. These figures illustrate that the thickness of the depleted silica layer is strongly dependent on D_H, and much less on D_{Ca}: whereas a variation of one order of magnitude of D_H is responsible for a threefold factor difference of the depth (h, corresponding to the distance at which the modeled curves reach 1) of the depleted silica layer ($h \sim 7$; 20 and 55 µm for $D_H = 10^{-13}$; 10^{-12} and 10^{-11} cm²/s, respectively), for a given value of D_H, h remains roughly constant despite discrepancies in D_{Ca} of up to four orders of magnitude. This observation is qualitatively consistent with the modeling of H^+-alkali interdiffusion (Hellmann 1997; Hellmann et al. 2003). The Ca profiles are not symmetric, unlike in the two aforementioned studies, because one of the interdiffusing cations is divalent, which in turn modifies the mathematical expression of $\widetilde{D}$. Also, the thinnest silica layers give rise to the sharpest chemical profiles. To reproduce layers with thickness of ~20 µm, values of D_H of ~10^{-12} cm²/s are required; however, the calculated Ca profiles are then not at all sharp, irrespective of the value of D_{Ca} (Fig. 7b). On the other hand, it is possible to generate sharper and sharper Ca gradients, but only if the total silica layer thickness is steadily reduced. An extrapolation of Figure 7c would show that the reproduction of ~20 µm thick silica layers with a sharper change in Ca concentration would require performing simulations with unrealistic D_H/D_{Ca} ratios. The most important conclusion borne out by our diffusion model is that the leached layer mechanism cannot reproduce both thick cation depleted silica layers, with a depth on the order of ~20 µm, in conjunction with nanometer-wide interfacial chemical gradients. Similar trends can be pointed out for wollastonite sample reacted in supercritical CO_2 (Figs. 8b, 8c, and 8d). In this latter case, these findings are thus also consistent with the idea that an H_2O thin fluid layer is required for the transport of calcium species from the wollastonite interface to the locations where calcite crystals precipitate.

Similar conclusions were previously reached by Hellmann et al. (2003). By comparing chemical profiles performed by secondary ion mass spectrometry (SIMS) with EFTEM, Hellmann et al. (2004) proposed that the profiles measured by techniques with low lateral spatial resolution, such as X-ray photoelectron spectroscopy (XPS) or SIMS, which are sigmoidal and therefore in agreement with leached layer theory, result from the integrated effects of both surface topography and laterally variable depths of surface chemical alteration. The combination of either the FIB-EFTEM or FIB-STEM-EDXS technique is therefore an invaluable method to circumvent this problem and allows the determination of the "true" chemical and structural profiles at the nanometer-scale, which were proposed to be consistent with an interfacial dissolution-precipitation mechanism by Hellmann et al. (2003). This mechanism is the most likely explanation for the formation of the silica layers in the case of wollastonite carbonation, as it explains the sharp interfaces, the elevated porosities, and the presence of secondary Ca-phyllosilicates. These 3 phenomena require the breakdown of all bonds at the wollastonite reaction front.

One can ask the question as to why wollastonite carbonation, via an interfacial dissolution-reprecipitation mechanism, leads to pseudomorphic features in the silica layer (the detailed preservation of the initial morphology of the grains by the silica coating, see Fig. 6a; see also Fig. 2e in Daval et al. 2009). Even though it is commonly assumed that only solid state transformations lead to pseudomorphic replacement, Putnis (2002) and Putnis and Putnis (2007) provide convincing evidence that dissolution-reprecipitation reactions are also compatible with pseudomorphism. We suggest that the pseudomorphic texture implies an intrinsic silica precipitation rate much greater than the dissolution reaction, this corresponding to a mechanism whereby silica entities that detach from the reactive wollastonite interface remain in the interfacial region and are immediately reprecipitated, thus facilitating the replication of the original wollastonite grain morphology. Such reasoning also justifies the use of an "infinitely" rapid precipitation rate of amorphous silica during the course of the kinetic modeling. Moreover, a trivial but interesting aspect of wollastonite carbonation is that silica is always in contact with wollastonite (but wollastonite is never in contact with calcite, nor with Ca-phyllosilicates). This may indicate that amorphous silica precipitates even faster than calcite or plombierite.

The comparison between the diffusion modeling results and the measured Ca profiles strongly supports the interfacial dissolution-reprecipitation mechanism for all of the experimental conditions investigated in this study, even in a supercritical CO_2 phase, where the mole fraction of water present in CO_2 at pCO_2 = 25 MPa is about 4‰ (Fig. 3 in Spycher et al. 2003). It would be interesting to determine whether there is a critical water fugacity, below which a switch from dissolution-reprecipitation to a presumably far slower solid-state diffusion mechanism might occur.

The role of silica coatings reported in the literature

As previously pointed out, the impact of silica coatings on the transport of solutes to and from the dissolving parent silicate phase has been a debated question for more than 40 years. Their occurrence on naturally weathered samples has been suggested to contribute at least partly to the long-standing problem of the orders of magnitude difference that exists between field and laboratory dissolution rates determined for single minerals (Nugent et al. 1998). Performing coupled dissolution-precipitation experiments in batch reactors represents a fruitful method of study "situated" between dissolution experiments in flow through reactors (which often are conducted at constant, far-from-equilibrium conditions) and dissolution in the field (which would include underground CO_2 sequestration sites) at conditions close to equilibrium. More specifically, the batch experiments used in this study mimic the non-constant (increasing) ΔG_r history of the carbonation process, and thus the sequential precipitation of different secondary phases, which ultimately are of importance in reproducing the correct temporal succession of microstructures. In the present study, we propose that the silica layers did not impede the transport of aqueous species to or from the wollastonite reaction interface. On the other hand, their passivating properties are rather attributed to the formation of secondary nano-precipitates (such as nano-calcites or Ca-phyllosilicates), occurring as a continuous surface coating and in pores and cracks within the silica layers.

With respect to silicate carbonation, a few studies have been published with contradictory results and interpretations. Huijgen et al. (2006) investigated the aqueous carbonation of wollastonite in ultrapure water, pCO_2 up to 4 MPa and T up to 225 °C. Unlike the present study, they proposed that the rate-limiting step of the process was the diffusion of Ca across a so-called leached layer. However, these authors claimed this without having performed comprehensive kinetic modeling of the process. Nonetheless, their estimates for the activation energy of the process, ranging from 16 to 22 kJ/mol, are in better agreement with a diffusion-limited process than one by chemical reactions at the wollastonite reaction front (Lasaga 1984). However, their estimated activation energies were extrapolated during the initial stages of dissolution (~15 min), a period during which steady-state conditions most probably were not attained, thus making their estimated E_a values suspect. Supporting our conclusions about attainment of steady-state rates, Weissbart and Rimstidt (2000) showed a significant, exponential decrease of the intrinsic wollastonite dissolution rate during the first five hours of the process. Such a transient period is often observed in silicate dissolution experiments conducted in mixed-flow reactor, and was proposed to result from the rapid disappearance of the most reactive sites (the corner ledges of grains) and/or the fast removal of fine particles that could adhere on the grains (see e.g., Hellmann 1995 for a thorough discussion).

The aqueous carbonation of Mg-bearing silicates has been the subject of many recent studies, in particular olivine (Mg_2SiO_4) and serpentine [$Mg_3Si_2O_5(OH)_4$]. With respect to olivine carbonation, Giammar et al. (2005) showed that the dissolution of olivine was continuously non-stoichiometric, characterized by the significant preferential release of Mg with respect to Si over a 3-week period (probably, the silica layer was not passivating). The study of Béarat et al. (2006) suggested that during olivine carbonation a passivating silica layer forms, based on experimental arguments and atomic level modeling. Specifically, their model hypothesizes that the silica layer consists exclusively of Si-O-Si bonds, without H species being present. One can note that similarities exist between those findings and a study of glass corrosion by Cailleteau et al. (2008), which advocates that the reorganization of the silica layer (via silanol condensation), in the absence of incorporated minor elements such as Zr in the silica matrix, results in pore closure and densification of the silica gel at the gel-solution interface.

A possible explanation for the passivating characteristics of silica layers is based on the nature of the cations present in the original mineral and whether or not these cations can be incorporated into the structure of the silica layer. With respect to the results of Béarat et al. (2006), it can perhaps be reasoned that Mg is not incorporated into the silica matrix (consistent with their modeling), thereby allowing gel reorganization and pore closure. Conversely, our results suggest that incorporation of Ca into the structure of the silica layer is possible (EELS measurement in Fig. 4c), such that this perhaps impedes densification and closure of the pores in the silica layer. We suggest that specific experiments should be conducted to investigate which cations affect the passivation characteristics of silica layers.

Studying serpentine carbonation, Park et al. (2004) also proposed that silica coatings act to kinetically slow down serpentine dissolution. They observed that grinding the grains enhanced the reaction rates, which they interpreted as resulting from the removal of the silica layers. However, it is more likely that the observed increase in the weathering rate of serpentine can be attributed to an increase of the total reactive surface area.

CONCLUDING REMARKS

On the whole, this rapid overview of several studies makes clear that the study of the role of silica coatings on the carbonation process is in its infancy, and that more work will be necessary to build up a comprehensive and consistent set of data, thereby permitting the construction of models to predict the variable passivation trends that have been measured in various studies.

The micro- to nanostructural aspects of carbonated wollastonite samples, based on a combination of focused ion beam milling and electron microscopy, were found to exhibit features that suggest that carbonation took place with a unique mechanism, both in aqueous solutions and in supercritical CO_2: dissolution-precipitation. Previous studies (Putnis 2002) have proposed that such a mechanism implies the development of porosity within the secondary phases only if the reaction pro-

ceeds with a "molar deficit," which is the case here. Nano-pores were observed within the silica layers surrounding the unaltered wollastonite grains. Calcium ions may play an important role in determining the structure of the silica layer; in the present study, we propose that the incorporation of minor amounts of Ca in the silica gel can partly prevent its reorganization, via condensation reactions such as:

$$\equiv Si\text{-}OH + HO\text{-}Si\equiv \rightarrow \equiv Si\text{-}O\text{-}Si\equiv + H_2O \quad (6)$$

The occurrence within the silica matrix of micrometer- to nanometer-sized cracks whose formation is most likely contemporaneous with the carbonation reactions (as revealed by the presence of calcite occasionally filling them), presumably constituted a network of channels for the inward and outward transport of aqueous species. The mechanism of formation of such cracks remains unclear; a possible explanation could be that cracks are the result of partial polymerization or dehydration of the silica gel, but more work is needed to support this idea.

Combining these observations at the nanometer-scale with macroscopic measurements of extents of carbonation as a function of time, and then comparing these results with kinetic modeling, results in the conclusion that the silica coatings that formed on the wollastonite grains did not significantly affect the aqueous carbonation rate. However, under conditions that favor the crystallization of small crystals (nano-crystallites), the coatings assume a potential passivating function, either because of pore and crack filling by calcite, or because the silica layer becomes overlain by a dense, homogeneous packing of small calcite crystals.

These novel findings bring new insights about the transport properties of coatings, and show that the methodology developed in the present study is suitable for investigating their overall role on mineral weathering rates. Comparing such an approach with microstructural modeling of secondary phases will help to determine whether the by-products of carbonation potentially passivate silicate surfaces, as well as to assess whether the geologic storage of CO_2 by mineral trapping (carbonate sequestration) will be a realistic solution for mitigating rising levels of anthropogenic CO_2 in the atmosphere.

ACKNOWLEDGMENTS

The authors thank A. Fernandez-Martinez (LGIT, Grenoble) for his valuable help with the treatment of the diffraction-line broadening performed on carbonated powders, as well as N. Menguy (IMPMC, Paris) for help with the acquisition of EELS spectra. We are also grateful to Region Ile-de-France for grants SESAME 2000 E1435 for the support to cryo-electron microscope JEOL 2100F and to Region Ile-de-France in the framework of C'nano IdF for the support to cryo-electron microscope JEOL 2100, both installed at IMPMC UMR 7590. This manuscript benefitted greatly from discussions with G. Montes-Hernandez (LGCA, Grenoble), S. Gin (CEA, Marcoule), and F. Brunet and V. Morales-Florez (ENS Géologie, Paris). Finally, we thank two anonymous reviewers for their helpful suggestions to improve the text. This is IPGP contribution no. 2534.

REFERENCES CITED

Andréani, M., Luquot, L., Gouze, P., Godard, M., Hoisé, E., and Gibert, B. (2009) Experimental study of carbon sequestration reactions controlled by the percolation of CO_2-rich brine through peridotites. Environmental Science and Technology, 43, 1226–1231.

Barlet-Gouédard, V., Rimmelé, G., Goffé, B., and Porcherie, O. (2007) Well technologies for CO_2 geological storage: CO_2-resistant cement. Oil and Gas Science and Technology, 62, 325–334.

Baucke F.G.K. (1974) Investigation of surface layers, formed on glass electrode membranes in aqueous solutions, by means of an ion sputtering method. Journal of Non-Crystalline Solids, 14, 13–31.

Béarat, H., McKelvy, M.J., Chizmeshya, A.V.G., Gormley, D., Nunez, R., Carpenter, R.W., Squires, K., and Wolf, G.H. (2006) Carbon sequestration via aqueous olivine mineral carbonation: Role of passivating layer formation. Environmental Science and Technology, 40, 4802–4808.

Berner, R.A. (1978) Rate control of mineral dissolution under Earth surface conditions. American Journal of Science, 278, 1235–1252.

Berner, R.A. and Holdren Jr., G.R. (1979) Mechanism of feldspar weathering, II. Observations of feldspars from soils. Geochimica et Cosmochimica Acta, 43, 1173–1186.

Berner, R.A., Sjoberg, E.L., Velbel, M.A., and Krom, M.D. (1980) Dissolution of pyroxenes and amphiboles during weathering. Science, 207, 1205–1206.

Berner, R.A., Lasaga, A.C., and Garrels, R.M. (1983) The carbonate-silicate cycle and its effect on atmospheric carbon dioxide over the past 100 millions years. American Journal of Science, 284, 641–683.

Benzerara, K., Menguy, N., Guyot, F., Vanni, C., and Gillet, P. (2005) TEM study of a silicate-carbonate-microbe interface prepared by focused ion beam milling. Geochimica et Cosmochimica Acta, 69, 1413–1422.

Bonaccorsi, E., Merlino, S., and Kampf, A.R. (2005) The crystal structure of tobermorite 14 Å (plombierite), a C-S-H phase. Journal of the American Ceramic Society, 88, 505–512.

Brady, J.B. (1995) Diffusion data for silicate minerals, glasses, and liquids. In T.J. Ahrens, Ed., Mineral Physics and Crystallography, 2, p. 269–290. AGU, Washington, D.C.

Brantley, S.L. (1992) Kinetics of dissolution and precipitation—Experimental and field results. In Y.K. Kharaka and K.S. Maest, Eds., Water–Rock Interaction, p. 3–6. Balkema, Rotterdam.

Burch, T.E., Nagy, K.L., and Lasaga, A.C. (1993) Free energy dependence of albite dissolution kinetics at 80 °C and pH 8.8. Chemical Geology, 105, 137–162.

Cagliotti, G., Paoletti, A., and Ricci, F.P. (1958) Choice of collimators for a crystal spectrometer for neutron diffraction. Nuclear Instruments and Methods, 3, 223–228.

Cailleteau, C., Angeli, F., Devreux, F., Gin, S., Jestin, J., Jollivet, P., and Spalla, O. (2008) Insight into silicate-glass corrosion mechanisms. Nature Materials, 7, 978–983.

Casey, W.H., Westrich, H.R., and Arnold, G.W. (1988) Surface-chemistry of labradorite feldspar reacted with aqueous-solutions at pH = 2, 3, and 12. Geochimica et Cosmochimica Acta, 52, 2795–2807.

Casey, W.H., Westrich, H.R., Banfield, J.F., Ferruzzi, G., and Arnold, G.W. (1993) Leaching and reconstruction at the surface leaching and reconstruction at the surfaces of dissolving chain-silicate minerals. Nature, 366, 253–256.

Cassou, C. (2000) Modélisation numérique des interactions eau-roche: Optimisation du code de calcul DIAPHORE et application à la diagenèse minérale des réservoirs, p. 188. Ecole nationale supérieure d'arts et métiers, Paris, France.

Chaïrat, C., Oelkers, E.H., Schott, J., and Lartigue, J.-E. (2007) Fluorapatite surface composition in aqueous solution deduced from potentiometric, electrokinetic, and solubility measurements, and spectroscopic observations. Geochimica et Cosmochimica Acta, 71, 5888–5900.

Chou, L. and Wollast, R. (1984) Study of the weathering of albite at room temperature and pressure with a fluidized bed reactor. Geochimica et Cosmochimica Acta, 48, 2205–2217.

Corvisier, J., Brunet, F., Fabbri, A., Bernard, S., Findling, N., Rimmelé, G., Barlet-Gouédard, V., Beyssac, O., and Goffé, B. (2009) Raman mapping and numerical simulation of calcium carbonates distribution in experimentally carbonated Portland cement cores. European Journal of Mineralogy, in press.

Crank, J. (1990) The Mathematics of Diffusion, 411 p. Oxford University Press, U.K.

Cubillas, P., Kohler, S., Prieto, M., Causserand, C., and Oelkers, E.H. (2005) How do mineral coatings affect dissolution rates? An experimental study of coupled $CaCO_3$ dissolution-$CdCO_3$ precipitation. Geochimica et Cosmochimica Acta, 69, 5459–5476.

Daval, D., Martinez, I., Corvisier, J., Findling, N., Goffé, B., and Guyot, F. (2009) Carbonation of Ca-bearing silicates, the case of wollastonite: Experimental investigations and kinetic modeling. Chemical Geology, 265, 63–78.

Dessert, C., Dupré, B., Gaillardet, J., François, L.M., and Allègre, C.J. (2003) Basalt weathering laws and the impact of basalt weathering on the global carbon cycle. Chemical Geology, 202, 257–273.

Doremus, R.H. (1975) Interdiffusion of hydrogen and alkali ions in a glass surface. Journal of Non-Crystalline Solids, 19, 137–144.

Drever, J.I. and Clow, D.W. (1995) Weathering rates in catchments. In A.F. White and S.L. Brantley, Eds., Chemical Weathering Rates of Silicate Minerals, 31, p. 463–483. Reviews in Mineralogy, Chantilly, Virginia.

Dufaud, F. (2006) Etude expérimentale des réactions de carbonatation minérale du CO_2 dans les roches basiques et ultrabasiques, 261 p. Ph.D. thesis, Institut de Physique du Globe de Paris.

Finger, L.W., Cox, D.E., and Jephcoat, A.P. (1994) A correction for powder diffraction peak asymmetry due to axial divergence. Journal of Applied Crystallography, 27, 892–900.

Gaillardet, J., Dupré, B., Louvat, P., and Allègre, C.J. (1999) Global silicate weathering and CO_2 consumption rates deduced from the chemistry of large rivers. Chemical Geology, 159, 3–30.

Giammar, D.E., Bruant, R.G., and Peters, C.A. (2005) Forsterite dissolution and magnesite precipitation at conditions relevant for deep saline aquifer storage and sequestration of carbon dioxide. Chemical Geology, 217, 257–276.

Gin, S., Ribet, I., and Couillard, M. (2001) Role and properties of the gel formed during nuclear glass alteration: Importance of gel formation conditions. Journal of Nuclear Materials, 298, 1–10.

Golubev, S.V., Pokrovsky, O.S., and Schott, J. (2005) Experimental determination of the effect of dissolved CO_2 on the dissolution kinetics of Mg and Ca silicates at 25 °C. Chemical Geology, 217, 227–238.

Green, E. and Lüttge, A. (2006) Incongruent dissolution of wollastonite measured with vertical scanning interferometry. American Mineralogist, 91, 430–434.

Hazen, R.M., Finger, L.W., Hemley, R.J., and Mao, H.K. (1989) High-pressure crystal chemistry and amorphization of alpha-quartz. Solid State Communications, 72, 507–511.

Heaney, P.J., Vicenzi, E.P., Giannuzzi, L.A., and Livi, K.J.T. (2001) Focused ion beam milling: A method of site-specific sample extraction for microanalysis of Earth and planetary materials. American Mineralogist, 86, 1094–1099.

Helgeson, H.C. (1971) Kinetics of mass transfer among silicates and aqueous solutions. Geochimica et Cosmochimica Acta, 35, 421–469.

——— (1972) Kinetics of mass transfer among silicates and aqueous solutions: Correction and clarification. Geochimica et Cosmochimica Acta, 36, 1067–1070.

Hellmann, R. (1995) The albite-water system Part II. The time-evolution of the stoichiometry of dissolution as a function of pH at 100, 200, and 300 °C. Geochimica et Cosmochimicta Acta, 59, 1669–1697.

——— (1997) The albite-water system. 4. Diffusion modeling of leached and hydrogen-enriched layers. Geochimica et Cosmochimica Acta, 61, 1595–1611.

——— (2007) Altération des minéraux en présence des fluides aqueux: Mécanismes, réactivité et processus, 315 p. Mémoire HDR Université Joseph Fourier, Grenoble.

Hellmann, R. and Tisserand, D. (2006) Dissolution kinetics as a function of the Gibbs free energy of reaction: An experimental study based on albite feldspar. Geochimica et Cosmochimica Acta, 70, 364–383.

Hellmann, R., Crerar, D.A., and Zhang, R. (1989) Albite feldspar hydrolysis to 300 °C. Solid State Ionics, 32/33, 314–329.

Hellmann, R., Dran, J.C., and DellaMea, G. (1997) The albite-water system. Part III. Characterization of leached and hydrogen-enriched layers formed at 300°C using MeV ion beam techniques. Geochimica et Cosmochimica Acta, 61, 1575–1594.

Hellmann, R., Penisson, J.-M., Hervig, R.L., Thomassin, J.-H., and Abrioux, M.-F. (2003) An EFTEM/HRTEM high-resolution study of the near surface of labradorite feldspar altered at acid pH: Evidence for interfacial dissolution-reprecipitation. Physics and Chemistry of Minerals, 30, 192–197.

Hellmann, R., Penisson, J.-M., Hervig, R.L., Thomassin, J.-H., and Abrioux, M.-F. (2004) Chemical alteration of feldspar: a comparative study using SIMS and HRTEM/EFTEM. In R.B. Wanty and R.R. Seal II, Eds., Water Rock Interaction, p. 753–756. A.A. Balkema, Rotterdam.

Huijgen, W.J.J., Witkamp, G.-J., and Comans, R.N.J. (2006) Mechanisms of aqueous wollastonite carbonation as a possible CO_2 sequestration process. Chemical Engineering Science, 61, 4242–4251.

Kasioptas, A., Perdikouri, C., Putnis, C.V., and Putnis, A. (2008) Pseudomorphic replacement of single calcium carbonate crystals by polycrystalline apatite. 8th International Symposium on the Geochemistry of the Earth's Surface (GES-8), p. 77–80. Mineralogical Society, London.

Kelemen, P.B. and Matter, J. (2008) In situ carbonation of peridotite for CO_2 storage. Proceedings of the National Academy of Sciences, 105, 17295–17300.

Knauss, K.G., Johnson, J.W., and Steefel, C.I. (2005) Evaluation of the impact of CO_2, co-contaminant gas, aqueous fluid and reservoir rock interactions on the geologic sequestration of CO_2. Chemical Geology, 217, 339–350.

Kump, L.R., Brantley, S.L., and Arthur, M.A. (2000) Chemical, weathering, atmospheric CO_2, and climate. Annual Review of Earth and Planetary Sciences, 28, 611–667.

Lagache, M. (1976) New data on the kinetics of the dissolution of alkali feldspars at 200 °C in CO_2 charged water. Geochimica et Cosmochimica Acta, 40, 157–161.

Lasaga, A.C. (1984) Chemical kinetics of water-rock interactions. Journal of Geophysical Research, 89, 4009–4025.

Lasaga, A.C. and Lüttge, A. (2001) Variation of crystal dissolution rate based on a dissolution stepwave model. Science, 291, 2400–2404.

Lasaga, A.C., Soler, J.M., Ganor, J., Burch, T.E., and Nagy, K.L. (1994) Chemical weathering rate laws and global geochemical cycles. Geochimica et Cosmochimica Acta, 58, 2361–2386.

Le Guen, Y., Renard, F., Hellmann, R., Collombet, M., Tisserand, D., Brosse, E., and Gratier, J.-P. (2007) Enhanced deformation of limestone and sandstone in the presence of a high P_{CO_2} fluids. Journal of Geophysical Research, 112, B05421.

Lee, M.R., Brown, D.J., Smith, C.L., Hodson, M.E., Mackenzie, M., and Hellmann, R. (2007) Characterization of mineral surfaces using FIB and TEM: A case study of naturally weathered alkali feldspars. American Mineralogist, 92, 1383–1394.

Luce, R.W., Bartlett, R.W., and Parks, G.A. (1972) Dissolution kinetics of magnesium silicates. Geochimica et Cosmochimica Acta, 36, 33–50.

Maeshima, T., Noma, H., Sakiyama, M., and Mitsuda, T. (2003) Natural 1.1 and 1.4 nm tobermorites from Fuka, Okayama, Japan: Chemical analysis, cell dimensions, ^{29}Si NMR and thermal behavior. Cement and Concrete Research, 33, 1515–1523.

Mamedov, K.S. and Belov, N.V. (1956) The crystal structure of wollastonite. Doklady Akademii Nauk SSSR, 107, 463–466.

Martinez-Blanco, D., Gorria, P., Blanco, J.A., Perez, M.J., and Campo, J. (2008) Analysis of the diffraction-line broadening on nanostructured Fe: size–strain effects induced by milling and heating. Journal of Physics: Condensed Matter, 20, 335213.

McGrail, P.B., Schaef, T.H., Ho, A.M., Chien, Y.-J., and Dooley, J.J. (2006) Potential for carbon dioxide sequestration in flood basalts. Journal of Geophysical Research, 111, B12201.

Messaoudi, C., Boudier, T., Sanchez-Sorzan, C.O., and Marco, S. (2007) TomoJ: tomography software for three-dimensional reconstruction in transmission electron microscopy. BMC Bioinformatics, 8(288), 1–9.

Montes-Hernandez, G. (2009) Experimental and numerical simulation of physico-chemical reactions at solid-fluid interfaces, 174 p. Mémoire HDR Université Joseph Fourier, Grenoble.

Montes-Hernandez, G., Fernandez-Martinez, A., Charlet, L., Tisserand, D., and Renard, F. (2008) Textural properties of synthetic nano-calcite produced by hydrothermal carbonation of calcium hydroxide. Journal of Crystal Growth, 310, 2946–2953.

Murphy, W.M. and Helgeson, H.C. (1989) Thermodynamic and kinetic constraints on reaction rates among minerals and aqueous solutions; IV, Retrieval of rate constants and activation parameters for the hydrolysis of pyroxene, wollastonite, olivine, andalusite, quartz, and nepheline. American Journal of Science, 289, 17–101.

Nugent, M.A., Brantley, S.L., Pantano, C.G., and Maurice, P.A. (1998) The influence of natural mineral coatings on feldspar weathering. Nature, 395, 588–591.

Oelkers, E.H., Schott, J., and Devidal, J.-L. (1994) The effect of aluminum, pH, and chemical affinity on the rates of aluminosilicate dissolution reactions. Geochimica et Cosmochimica Acta, 58, 2011–2024.

Oelkers, E.H., Gislason, S.R., and Matter, J. (2008) Mineral carbonation of CO_2. Elements, 4, 333–337.

Park, A.-H.A., and Fan, L.-S. (2004) CO_2 mineral sequestration: physically activated dissolution of serpentine and pH swing process. Chemical Engineering Science, 59, 5241–5247.

Park, A.-H.A., Jadhav, R., and Fan, L. (2003) CO_2 mineral sequestration: Chemically enhanced aqueous carbonation of serpentine. Canadian Journal of Chemical Engineering, 81, 885–890.

Petit, J.C., Dellamea, G., Dran, J.C., Magonthier, M.C., Mando, P.A., and Paccagnella, A. (1990) Hydrated-layer formation during dissolution of complex silicate-glasses and minerals. Geochimica et Cosmochimica Acta, 54, 1941–1955.

Putnis, A. (2002) Mineral replacement reactions: from macroscopic observations to microscopic mechanisms. 18th General Meeting of the International Mineralogical Association, p. 689–708. Mineralogical Society, Edinburgh, Scotland.

Putnis, A. and Putnis, C.V. (2007) The mechanism of reequilibration of solids in the presence of a fluid phase. Journal of Solid State Chemistry, 180, 1783–1786.

Putnis, C.V., Tsukamoto, K., and Nishimura, Y. (2005) Direct observations of pseudomorphism: Compositional and textural evolution at a fluid-solid interface. American Mineralogist, 90, 1909–1912.

Rasband, W. (2002) ImageJ: Image Processing and Analysis in Java. NIH; available online at http://rsb.info.nih.gov/ij/docs/intro.html.

Raudsepp, M., Pani, E., and Dipple, G.D. (1999) Measuring mineral abundance in skarn I: The Rietveld method using X-ray powder diffraction data. Canadian Mineralogist, 37, 1–15.

Richardson, I.G. (2008) The calcium silicate hydrates. Cement and Concrete Research, 38, 137–158.

Rimmelé, G., Barlet-Gouédard, V., Porcherie, O., Goffé, B., and Brunet, F. (2008) Heterogeneous porosity distribution in Portand cement exposed to CO_2-rich fluids. Cement and Concrete Research, 38, 1038–1048.

Rimstidt, J.D. and Dove, P.M. (1986) Mineral/solution reaction rates in a mixed flow reactor: Wollastonite hydrolysis. Geochimica et Cosmochimica Acta, 50, 2509–2516.

Rodríguez-Carvajal, J. (2001) An introduction to the program Fullprof 2000. Gif sur Yvette. http://www.ill.eu/sites/fullprof/php/tutorials.html

Schott, J., Berner, R.A., and Lennart Sjöberg, E. (1981) Mechanism of pyroxene and amphibole weathering—I. Experimental studies of iron-free minerals. Geochimica et Cosmochimica Acta, 45, 2123–2135.

Schweda, P., Sjöberg, L., and Södervall, U. (1997) Near-surface composition of acid-leached labradorite investigated by SIMS. Geochimica et Cosmochimica Acta, 61, 1985–1994.

Shih, S.M., Ho, C.S., Song, Y.S., and Lin, J.P. (1999) Kinetics of the reaction of $Ca(OH)_2$ with CO_2 at low temperature. Industrial and Engineering Chemistry

Research, 38, 1316–1322.
Shiraki, R. and Brantley, S.L. (1995) Kinetics of near-equilibrium calcite precipitation at 100 °C: An evaluation of elementary reaction-based and affinity-based rate laws. Geochimica et Cosmochimica Acta, 59, 1457–1471.
Sitepu, H., O'Connor, B.H., and Li, D. (2005) Comparative evaluation of the March and generalized spherical harmonic preferred orientation models using X-ray diffraction data for molybdite and calcite powders. Journal of Applied Crystallography, 38, 158–167.
Spycher, N., Pruess, K., and Ennis-King, J. (2003) CO_2-H_2O mixtures in the geological sequestration of CO_2. I. Assessment and calculation of mutual solubilities from 12 to 100 °C and up to 600 bar. Geochimica et Cosmochimica Acta, 67, 3015–3031.
Swoboda-Colberg, N.G. and Drever, J.I. (1993) Mineral dissolution rates in plot-scale field and laboratory experiments. Chemical Geology, 150, 51–69.
Teir, S., Kuusik, R., Fogelhohn, C.J., and Zevenhoven, R. (2007) Production of magnesium carbonates from serpentinite for long-term storage of CO_2. International Journal of Mineral Processing, 85, 1–15.
Thompson, P., Cox, D.E., and Hastings, J.B. (1987) Rietveld refinement of Debye-Scherrer synchrotron X-ray data from Al_2O_3. Journal of Applied Crystallography, 20, 79–83.
van der Lee, J. and De Windt, L. (2002) CHESS Tutorial and Cookbook. Updated for version 3.0, 116 p. Ecole des Mines de Paris Centre d'Informatique Geologique Fontainebleau, France.
Velbel, M.A. (1993) Formation of protective surface layers during silicate-mineral weathering under well-leached, oxidizing conditions. American Mineralogist, 78, 405–414.
Viswamitra, M.A. and Jayalakshmi, R.K. (1972) Thermal vibrations and melting point-NaCl and KCl. Acta Crystallographica Section A, A28, S189–S190.
Walker, J.C.G., Hays, P.B., and Kasting, J.F. (1981) A negative feedback mechanism for the long-term stabilization of Earth's surface temperature. Journal of Geophysical Research, 86, 9776–9782.
Weissbart, E.J. and Rimstidt, D.J. (2000) Wollastonite: Incongruent dissolution and leached layer formation. Geochimica et Cosmochimica Acta, 64, 4007–4016.
White, A.F. and Brantley, S.L. (1995) Chemical weathering rates of silicate minerals: An overview. In A.F. White and S.L. Brantley, Eds., Chemical Weathering Rates of Silicate Minerals, 31, p. 1–22. Reviews in Mineralogy, Mineralogical Society of America, Chantilly, Virginia.
——— (2003) The effect of time on the weathering of silicate minerals: Why do weathering rates differ in the laboratory and field? Chemical Geology, 202, 479–506.
White, A.F., Bullen, T.D., Schulz, M.S., Blum, A.E., Huntington, T.G., and Peters, N.E. (2001) Differential rates of feldspar weathering in granitic regoliths. Geochimica et Cosmochimica Acta, 65, 847–869.
Wirth, R. (2004) Focused ion beam (FIB): A novel technology for advanced application of micro- and nanoanalysis in geosciences and applied mineralogy. European Journal of Mineralogy, 16, 863–876.
——— (2009) Focused Ion Beam (FIB) combined with SEM and TEM: Advanced analytical tools for studies of chemical composition, microstructure and crystal structure in geomaterials on a nanometer scale. Chemical Geology, 261, 217–229.
Xie, Z. and Walther, J.V. (1994) Dissolution stoichiometry and adsorption of alkali and alkaline earth elements to the acid-reacted wollastonite surface at 25 °C. Geochimica et Cosmochimica Acta, 58, 2587–2598.
Xu, T., Apps, J.A., and Pruess, K. (2004) Numerical simulation of CO_2 disposal by mineral trapping in deep aquifers. Applied Geochemistry, 19, 917–936.

Manuscript received May 20, 2009
Manuscript accepted August 3, 2009
Manuscript handled by Bryan Chakoumakos

Daval et al. Deposit AM-09-053 Appendix A Nov/Dec 2009 American Mineralogist

The goal of the present section is to show that the size of the critical nuclei is smaller in experiments conducted in alkaline solution compared to water. First, one can express the quantity of carbonate ion for the two experiments (carbonation in water, alkaline solution) as follows:

$$[CO_3^{2-}]^{wat}_{eq} < [CO_3^{2-}]^{alk}_{eq} \quad \text{(A1)}$$

where $[CO_3^{2-}]^{wat}_{eq}$ and $[CO_3^{2-}]^{alk}_{eq}$ represent the concentration of CO_3^{2-} species in equilibrium with calcite under constant CO_2 fugacity, in water and in the alkaline solution, respectively. The time needed for achievement of calcite saturation is considered arbitrary, and is called t_0 in both cases. Because the initial pH values of both solutions were 3.1 and 5.6 (water and alkaline solution, respectively), and assuming that wollastonite dissolution rates are independent of pH in the range 2–6 (Weissbart and Rimstidt 2000), then over an infinitesimal interval of time Δt, the same amount of calcium (Δn_{Ca}^{wat} and Δn_{Ca}^{alk}, respectively) is released to the fluid by wollastonite dissolution at each condition:

$$\Delta n_{Ca}^{wat} = \Delta n_{Ca}^{alk} \quad \text{(A2)}$$

Multiplying the left and right terms of Equation A1 by the respective number of incremental moles of Ca released (Eq. A2), and dividing by the volume, yields:

$$(\Delta n_{Ca}^{wat}/V_f) \times [CO_3^{2-}]^{wat}_{eq} < [CO_3^{2-}]^{alk}_{eq} \times (\Delta n_{Ca}^{alk}/V_f) \quad \text{(A3)}$$

If activities are equated with aqueous concentrations, and the activity of calcite is unity, one can write:

$$K_s = [Ca^{2+}]^{wat}_{eq} \times [CO_3^{2-}]^{wat}_{eq} = [Ca^{2+}]^{alk}_{eq} \times [CO_3^{2-}]^{alk}_{eq} \quad \text{(A4)}$$

where $[Ca^{2+}]^{wat}_{eq}$ and $[Ca^{2+}]^{alk}_{eq}$ are the concentration of Ca^{2+} species in equilibrium with calcite under constant CO_2 fugacity, in water and in the alkaline solution, respectively, and K_s is the equilibrium constant for the reaction:

$$CaCO_3 \rightarrow Ca^{2+} + CO_3^{2-} \quad \text{(A5)}$$

Summing Equations A3 and A4, and rearranging the carbonate terms, results in:

$$[CO_3^{2-}]^{wat}_{eq} \times (\Delta n_{Ca}^{wat}/V_f + [Ca^{2+}]^{wat}_{eq}) < [CO_3^{2-}]^{alk}_{eq} \times (\Delta n_{Ca}^{alk}/V_f + [Ca^{2+}]^{alk}_{eq}) \quad \text{(A6)}$$

At this stage, each side of Equation A6 nearly represents the ion activity product of Equation A5 at $t_0 + \Delta t$ in water and in alkaline solution, respectively, a point at which the fluid is supersaturated with respect to calcite, although it has not yet formed. This is, however, not exactly correct because the release of Δn_{Ca}^{wat} (or Δn_{Ca}^{alk}) to the respective solutions is necessarily accompanied by a pH increase and a concomitant modification of the fluid speciation. As revealed in Table 1, the carbonation reaction in both cases (water, alkaline solution) takes place at $pH < pKa_1 << pKa_2$

[where pKa_1 and pKa_2 stand for the pKa of the reactions $CO_2 + H_2O \rightarrow HCO_3^- + H^+$ and $HCO_3^- \rightarrow CO_3^{2-} + H^+$, respectively, equal to 6.39 and 10.08 at 100 °C (CHESS ref.)]. Thus, in this acidic to circum-neutral pH range, the main effect of the consumption of protons by the dissolution step will be the decomposition of carbonic acid and production of HCO_3^- species, while the concentration of CO_3^{2-} species will remain approximately the same. Therefore, the following approximations can be considered as reasonable:

$$[CO_3^{2-}]^{wat}_{eq} + (\Delta n_{CO3}{}^{wat}/V_f) \approx [CO_3^{2-}]^{wat}_{eq} \qquad \text{(A7a)}$$

$$[CO_3^{2-}]^{alk}_{eq} + (\Delta n_{CO3}{}^{alk}/V_f) \approx [CO_3^{2-}]^{alk}_{eq} \qquad \text{(A7b)}$$

where $\Delta n_{CO3}{}^{wat}$ and $\Delta n_{CO3}{}^{alk}$ are the amount of CO_3^{2-} species produced when $\Delta n_{Ca}{}^{wat}$ and $\Delta n_{Ca}{}^{alk}$ are released in water and in the alkaline solution respectively. Substituting $[CO_3^{2-}]^{wat}_{eq}$ and $[CO_3^{2-}]^{alk}_{eq}$ in Equation A6 by their values taken from Equations A7a and A7b, assuming that aqueous species concentrations are equivalent to activities and knowing that at $t_0 + \Delta t$, the fluid is supersaturated with respect to calcite, leads to:

$$0 < \Delta G_r(CaCO_3)_{t0+\Delta t}{}^{wat} < \Delta G_r(CaCO_3)_{t0+\Delta t}{}^{alk} \qquad \text{(A8)}$$

where $\Delta G_r(CaCO_3)_{t0+\Delta t}{}^{wat}$ and $\Delta G_r(CaCO_3)_{t0+\Delta t}{}^{alk}$ are the Gibbs free energy of calcite dissolution at $t_0 + \Delta t$ in water and in the alkaline solution, respectively. Thus, the incremental dissolution of wollastonite results in a higher degree of calcite supersaturation in the alkaline solution compared to water. Two important consequences follow from this result. First, as the critical radius (r_c) of a simple spherical nucleus is given by:

$$r_c = 2\gamma/\Delta G_r \qquad \text{(A9)}$$

where γ is its surface tension, then, the combination of Equations A8 and A9 yields:

$$r_c{}^{alk} < r_c{}^{wat} \qquad \text{(A10)}$$

The difference in the critical radii may explain why calcite is more prevalent in the silica layer (nano-crystallites in pores and cracks) when carbonation takes place in an alkaline solution compared to water. Such crystals could in turn fill up the pores and cracks in experiments with alkaline fluid. Secondly, larger initial supersaturations lead to faster nucleation rates, which translates into more numerous and smaller crystal sizes. Similar reasoning could be used for the precipitation of C-S-H phases, leading to the same consequences as the ones described above with respect to the silica layer.

Appendix B

The purpose of the present section is to detail how the general diffusion equation (Eq. 4) can be solved, supposing that: (1) the rate of retreat of the fluid–solid interface is nul ($a = 0$, see section "Mechanism of silica layer formation" for details), and (2) the outward diffusion of cations Ca^{2+} and the inward diffusion of H^+ are coupled by an ion exchange reaction between H^+

and M^{n+} species.

The expression below can be used to describe binary cation diffusion behavior in silicate minerals (from Brady 1995; see original references therein):

$$\tilde{D} = D_{A_bB_{-a}} = \left[\frac{D^*_{AZ} D^*_{BZ} (aN_{AZ} + bN_{BZ})^2}{a^2 N_{AZ} D^*_{AZ} + b^2 N_{BZ} D^*_{BZ}} \right] \times \left[1 + \left(\frac{\partial \ln \gamma_{AZ}}{\partial \ln N_{AZ}} \right)_{P,T} \right] \quad \text{(A11)}$$

where the reaction is $A_z^{+a} Z_a^{-z} \rightarrow B_z^{+b} Z_b^{-z}$, D_{AZ}^* and D_{BZ}^* are the respective tracer diffusion coefficients for phases *AZ* and *BZ,* and N_{AZ} and N_{BZ} are the mole fractions for each phase. Neglecting the activity coefficient of Equation A11 ($\gamma_{AZ} \approx 1$, see details in Hellmann 1997), the diffusion coefficient describing interdiffusion of monovalent species (H^+) for divalent species (Ca^{2+}) is given by the following simplified expression:

$$\tilde{D} = \frac{D_{Ca} D_H (C+1)^2}{4 D_{Ca} C + D_H (1-C)} \quad \text{(A12)}$$

D_H is the diffusion coefficient of H^+. Due to the non-linearity of the $\tilde{D}$ expression in terms of concentration and consequently depth, solving Equation 4 analytically is difficult. However, this equation can be linearized and then solved numerically using a finite-volume approach and implicit-explicit discretization. Theoretical Ca gradients are numerically approximated by the general following equation:

$$C_i^{n+1} = C_i^n + \frac{\Delta t}{\Delta x^2} \left(d_{i+1}^n C_{i+1}^{n+1} - (d_{i+1}^n + d_i^n) C_i^{n+1} + d_i^n C_{i-1}^{n+1} \right) \quad \text{(A13)}$$

where Δx and Δt are infinitesimal space and time intervals respectively, C_i^n is the concentrations of Ca at time *t* and at depth *x*, C_i^{n+1}, C_{i+1}^{n+1}, and C_{i-1}^{n+1} are the concentrations of Ca at time $t + \Delta t$ and at depth *x*, $x + \Delta x$ and $x - \Delta x$, respectively. The parameter d_i^n represents the diffusion coefficient at the boundary between two adjacent meshes at depths $x - \Delta x$ and *x*, respectively, and for the time *t*. These boundary diffusion coefficients can then be calculated from the values of the interdiffusion coefficients in each mesh (see Cassou 2000 for further explanations):

$$\begin{cases} d_1^n = \tilde{D}_1^n \\ d_i^n = \dfrac{\tilde{D}_{i-1}^n \tilde{D}_i^n (\Delta x + \Delta x)}{\tilde{D}_{i-1}^n \Delta x + \tilde{D}_i^n \Delta x} = \dfrac{2 \times \tilde{D}_{i-1}^n \tilde{D}_i^n}{\tilde{D}_{i-1}^n + \tilde{D}_i^n} \quad \forall i \in [2, N] \\ d_{N+1}^n = 0 \end{cases} \quad \text{(A14)}$$

where $\tilde{D}_i^n$ is the interdiffusion within the i^{th} mesh, and *N* is the total number of considered meshes during the course of the numerical simulation. This last expression takes into account the boundary conditions described earlier: there is a constant concentration at the "in-"boundary

flux of the first mesh and no flux at the "out-"boundary of the N^{th} mesh. Finally, the calculation of C_i^{n+1} consists in solving the following system of Equation A15a which also comprises the initial conditions of Equation A15b:

$$\begin{cases} C_1^{n+1} + \dfrac{\Delta t}{\Delta x^2}\left(-d_2^n C_2^{n+1} + (d_2^n + d_1^n)C_1^{n+1}\right) = C_1^n \\ C_i^{n+1} + \dfrac{\Delta t}{\Delta x^2}\left(-d_{i+1}^n C_{i+1}^{n+1} + (d_{i+1}^n + d_i^n)C_i^{n+1} - d_i^n C_{i-1}^{n+1}\right) = C_i^n, \forall i \in \left[2, N\right[\\ C_N^{n+1} + \dfrac{\Delta t}{\Delta x^2}\left(d_N^n C_N^{n+1} - d_N^n C_{N-1}^{n+1}\right) = C_N^n \end{cases} \quad \text{(A15a)}$$

$$C_i^1 = 1 \quad \forall i \in [1, N] \quad \text{(A15b)}$$